Improving 2-D Resolution in Geosynchronous SAR via Spatial Spectrum Synthesis: Method and Verification

Xinyan Chen, Zhiyang Chen, *Member, IEEE*, Yuanhao Li, *Member, IEEE*, Cheng Hu, *Senior Member, IEEE*, Xichao Dong, *Member, IEEE*, and Stephen Hobbs, *Member, IEEE*

***Abstract*—Geosynchronous synthetic aperture radar (GEO SAR) has the advantages of a short revisit time and a large beam footprint. Enhancing spatial resolution has become a hotspot in spaceborne SAR research areas. The existing designs of GEO SAR suffer from the problem of poor resolution (greater than 10 m) and cause low-precision observation in urban areas. First time, this article points out that GEO SAR has the ability to improve the two-dimensional (2-D) resolution of SAR images by spatial spectrum synthesis based on 2-D baselines, and proposes models and a signal processing method involved in GEO SAR spectrum synthesis. The 2-D spatial baselines of GEO SAR are analyzed and evaluated first based on satellite software and real ephemeris from Beidou Inclined Geosynchronous Orbit (IGSO) navigation satellites to demonstrate the potential of 2-D resolution improvement. Then the analytical models of the spectral shape and relative spectral shift between GEO SAR images are derived. Furthermore, a 2-D spectrum synthesis algorithm suitable for GEO SAR is also proposed, where we use deramping operation instead of the traditional spectrum shifting process. Nonideal factors are considered in the processing of synthesized. In addition, performances of the proposed algorithm, including the resolution improvement factor, the amplitude fluctuation, and the critical baseline, are constructed. Finally, computer simulations and equivalent experiments based on Beidou IGSO navigation satellites verify the proposed algorithm.**

***Index Terms*—Geosynchronous synthetic aperture radar (GEO SAR), resolution improvement, spatial spectrum synthesis, two-dimensional (2-D) spatial baseline.**

Manuscript received 9 March 2023; revised 4 October 2023; accepted 17 January 2024. Date of publication 1 February 2024; date of current version 8 March 2024. This work was supported in part by the National Natural Science Foundation of China under Grant 61960206009, Grant 62201051, and Grant 62101039, in part by the Shandong Excellent Young Scientists Fund Program (Overseas), in part by the Natural Science Foundation of Shandong Province under Grant ZR2022QF067, and in part by the National Key Research and Development Program of China under Grant SQ2022YFB3900055. *(Corresponding author: Zhiyang Chen.)*

Xinyan Chen, Yuanhao Li, and Cheng Hu are with the Radar Research Laboratory, School of Information and Electronics, Beijing Institute of Technology, Beijing 100081, China, and also with the Key Laboratory of Electronic and Information Technology in Satellite Navigation, Ministry of Education, Beijing Institute of Technology, Beijing 100081, China (e-mail: chenxinyan1998@163.com; lyh.900101@163.com; cchchb@163.com).

Zhiyang Chen is with the Radar Research Laboratory, School of Information and Electronics, Beijing Institute of Technology, Beijing 100081, China, also with the Key Laboratory of Electronic and Information Technology in Satellite Navigation, Ministry of Education, Beijing Institute of Technology, Beijing 100081, China, and also with the Advanced Technology Research Institute, Beijing Institute of Technology, Jinan 250300, China (e-mail: zychen12@163.com).

Xichao Dong is with the Radar Research Laboratory, School of Information and Electronics, Beijing Institute of Technology, Beijing 100081, China, and also with the Beijing Institute of Technology Chongqing Innovation Center, Chongqing 401120, China (e-mail: xcdong@foxmail.com).

Stephen Hobbs is with the School of Aerospace Transport and Manufacturing, Cranfield University, MK43 0AL Bedford, U.K. (e-mail: s.e.hobbs@cranfield.ac.uk).

Digital Object Identifier 10.1109/JSTARS.2024.3361165

I. Introduction

GEOSYNCHRONOUS synthetic aperture radar (GEO SAR) is a spaceborne SAR system operating in geosynchronous orbit at an altitude of 36 000 km [1]. The first GEO SAR satellite in the world, Ludi Tance-4 (01), was launched successfully on August 13, 2023. The master payload of this satellite is the *L*-band SAR system [2]. Compared with the traditional low-earth orbit SAR (LEO SAR), it has the advantages of a short revisit period (several hours to one day) and a large beam footprint (bringing in over 1000 km in imaging swath) [3]. Therefore, it plays a significant role in disaster prevention, e.g., geological disasters [4]. The research works in GEO SAR cover system design [5], [6], analysis of imaging influence factors [7], [8], [9], imaging algorithm [10], [11], [12], and subsequent processing, e.g., interferometry and tomography [13], [14], [15].

Recent research trends in spaceborne SAR include large constellations, high-resolution performance, and dimension detection [16], [17]. Among these, the requirement of high resolution is one of the core performance indices of the spaceborne SAR system. Therefore, it is an attractive research topic in the field of spaceborne SAR.

However, due to the main purposes for large-scale imaging and measurement including deformation retrieval [18] and atmosphere measurement [19], the existing GEO SAR concepts suffer from the problem of poor resolution (greater than 10 m). Typically, Madson's proposed scheme can obtain images with a resolution of 10 m and 50 m from the strip mapping mode and scan-SAR mode, respectively [20]. As for measurement, typical *L*-band and *C*-band GEO SAR systems were designed for earthquake deformation retrieval and integrated water vapor measurement with the resolution of 30 m and 500 m in the GESS and G-CLASS programs, respectively [18], [19]. The low-resolution performance of these existing GEO SAR systems reduces the high-precision observations in urban areas or high-resolution topographic mapping.

Thanks to the short revisit period and large beam footprint of GEO SAR, the lack of coarse resolution can be made up by a big

© 2024 The Authors. This work is licensed under a Creative Commons Attribution-NonCommercial-NoDerivatives 4.0 License. For more information, see https://creativecommons.org/licenses/by-nc-nd/4.0/

dataset. 1) The rapid revisit of GEO SAR enables it to acquire a large amount of observation data in a short time [21]. In addition, note that all targets suffer from temporal decorrelation (the scattering properties of targets vary with time), thus the shorter the revisit time of radar, the higher the temporal coherence. Therefore, the images acquired by GEO SAR also have a high coherence compared to LEO SAR images. 2) The large beam footprint of GEO SAR enables it to generate a two-dimensional (2-D) baseline without beam adjustment. This makes it possible to improve the image resolution by a multiframe image information fusion method based on spatial spectrum synthesis [22], which is to generate a larger 2-D) bandwidth by synthesizing the spectrums of SAR images obtained from different perspectives.

The concept of spatial spectrum synthesis was first proposed by Prati and Rocca [22] to improve range resolution by combining several SAR images from different perspectives. The relationship between angular separation and spectral shift was discussed for monostatic and bistatic SAR interferometers and further exploited to improve interferometry techniques by Gatelli [23]. This concept was later used on a LEO SAR constellation idea, i.e., Interferometric Cartwheel, to improve 2-D resolution by Massonnet [24]. Based on [22], for improving range-direction resolution, the effective baseline component was derived and a data processing method was proposed by Xu et al. [25]. The spectrum synthesis method was also used in other bistatic/multistatic SAR, such as the GEO spaceborne–airborne bistatic SAR system by Zheng et al. [26], multiple-input multiple-output distributed SAR system by Pastina et al. [27], GEO bistatic SAR system with a LEO receiver by Cheng et al. [28], and spaceborne-airborne multistatic SAR platform by Mao et al. [29]. The application of spectrum synthesis on the monostatic GEO SAR platform has not been involved yet.

Note that the existing research works mentioned above are based on airborne, LEO SAR, or bistatic/multistatic platforms, and they apply to the cases where radar works in broadside looking mode. However, the above methods are not suitable for GEO SAR, which usually works in squint mode.

Aiming at the characteristics of 2-D spatial baselines and squint mode for GEO SAR, this article proposes new vector models, nonideal factor analysis, and a signal processing method involved in GEO SAR spectrum synthesis. The main contributions of this article are as follows.

1) The potential of the resolution-improving method for monostatic GEO SAR via spectrum synthesis is demonstrated, in particular. For complex imaging geometry of GEO SAR, a new vector model and a complete processing for spectrum synthesizing including an equivalent shifting operation are proposed.
2) Nonideal factors such as temporal decorrelation and atmospheric turbulence are considered in SAR images to be synthesized. The comparison simulations show that nonideal factors cause defocusing in synthesized images of LEO SAR, working in *L*- and *X*-band, which verifies the advantages of daily *L*-band GEO SAR for spectral synthesizing.
3) Equivalent experiments based on Beidou Inclined Geosynchronous Orbit (IGSO) navigation satellites are conducted to verify the proposed resolution-improving algorithm and analysis for the first time.

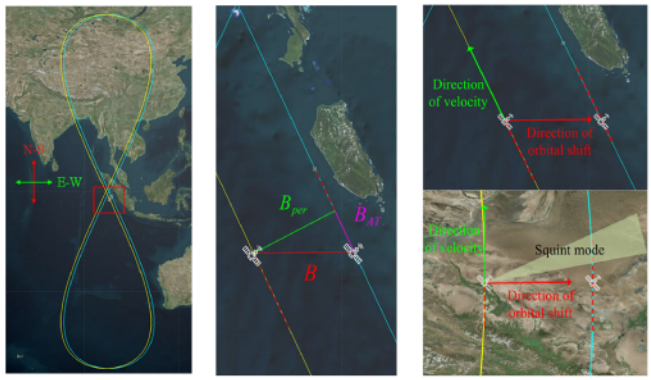

Fig. 1. (a) Nadir-point trajectory. (b) 2-D spatial baseline of GEO SAR. (c) Two sources of GEO SAR 2-D baseline.

The rest of this article is organized as follows. In Section II, we simulate and analyze the long-term motion of the GEO SAR satellite, which shows that a large 2-D spatial baseline can be generated, and proves the potential of improving 2-D resolution based on spatial spectrum synthesis. In Section III, we analyze the shape of the spatial spectrum and derive a new vector model of the spatial-spectral shift between repeated-track images. We improve the original spectrum synthesis algorithm flow, that is to use the deramping operation instead of the spectrum shifting process. Besides, we discussed the impact of nonideal factors such as SNR, temporal decorrelation, and atmospheric turbulence in the synthesizing processing. In Section IV, we construct evaluation models including the resolution improvement factor, the amplitude fluctuation, and the critical baseline. In Section V, the feasibility and performance analysis of the algorithm is verified by computer simulations and equivalent experiments based on IGSO navigation satellites.

II. 2-D Spatial Baseline of GEO SAR

2-D spatial baselines can be formed by repeated tracks in GEO SAR, as shown in Fig. 1(a). The yellow line and the blue line respectively represent the nadir-point trajectory of GEO SAR repeat tracks in two successive days. The 2-D spatial baselines are indicated in Fig. 1(b), where $B_{\rm per}$ is the perpendicular baseline and $B_{\rm AT}$ is the along-track baseline. As shown in Fig. 1(c), there are two main sources of GEO SAR 2D baseline.

1) The direction of the orbital shift caused by the Earth's rotation is not necessarily perpendicular to the direction of the velocity of GEO SAR. Operating in the high altitude of geosynchronous orbit, the GEO SAR will be severely affected by a series of perturbations [30], such as the third body gravity and aspheric gravity. Under the influence of the perturbations, the orbital elements of GEO SAR will constantly change with time, resulting in repeated tracks to shift in the East–West direction. However, the velocity of radar varies with the position of the track, thus there are many locations where the baseline is 2-D. For example, as

TABLE I
ORBITAL ELEMENTS OF BEIDOU SATELLITES AND GEO SAR

Orbital Element	GEO SAR	IGSO2	IGSO3	IGSO4	IGSO5
Semimajor Axis (km)	42 164	42 149	42 146	42 159	42 156
Inclination (deg)	53	53.6	57.6	54.5	53.5
Argument of Perigee (deg)	270	204.6	203.7	209.7	209.0
Eccentricity	0	0.005	0.003	0.004	0.004
RAAN (deg)	270	315.7	75.1	199.6	313.1

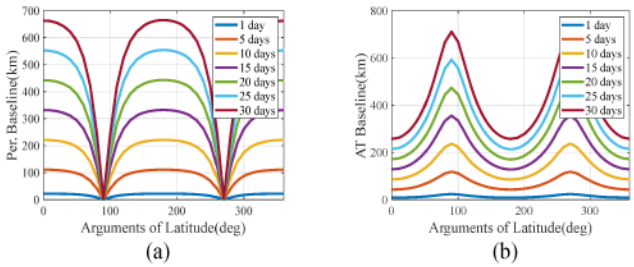

Fig. 2. Span of spatial baseline of GEO SAR. (a) Perpendicular baseline. (b) Along-track baseline.

shown in the upper part of Fig. 1(c), the velocity direction is not perpendicular to the orbital shift, resulting in 2-D baselines.

2) Squint mode is common in GEO SAR [31]. Even if the directions of the orbital shift and velocity are perpendicular, it can also generate a 2-D baseline since the beam is not broadside looking.

To demonstrate the potential of GEO SAR to improve 2-D resolution of images by 2-D spatial baselines, we simulate the baseline of the GEO SAR satellite under the influence of the perturbations by using the high-precision orbit propagator model in System Tool Kit software. The system parameters of GEO SAR are given in Table I. The Nadir-point trajectory of GEO SAR is shown in Fig. 1(a).

We selected the first day's track as a reference track and calculated the spatial baseline in cross-track and along-track directions of the remaining repeated tracks relative to the reference track. We analyzed the span of the perpendicular baseline and along-track baseline over a 30-day period at different arguments of latitude, as shown in Fig. 2. It can be seen that the closer the satellites to the polar, the more rapidly the along-track baselines increase since the orbit gradually drifts along the azimuth direction.

Considering that the orbital elements of Beidou IGSO navigation satellites and GEO SAR are highly similar [32], we also calculate the 2-D baseline of repeated tracks of several Beidou IGSO satellites based on their real ephemeris. The orbital elements of Beidou IGSO satellites are given in Table I. It can be seen that, for the two systems, their semimajor axes, inclinations, and eccentricities are very similar. The Nadir-point trajectories of the Beidou IGSO satellites are shown in Fig. 3. The 2-D baselines at two typical orbital positions (near the Equator and near the pole) are shown in Fig. 4.

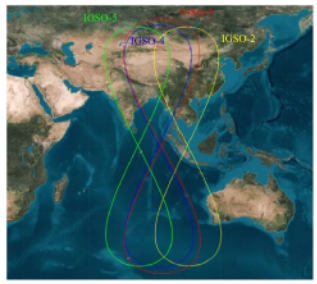

Fig. 3. Nadir-point trajectory of Beidou IGSO satellites.

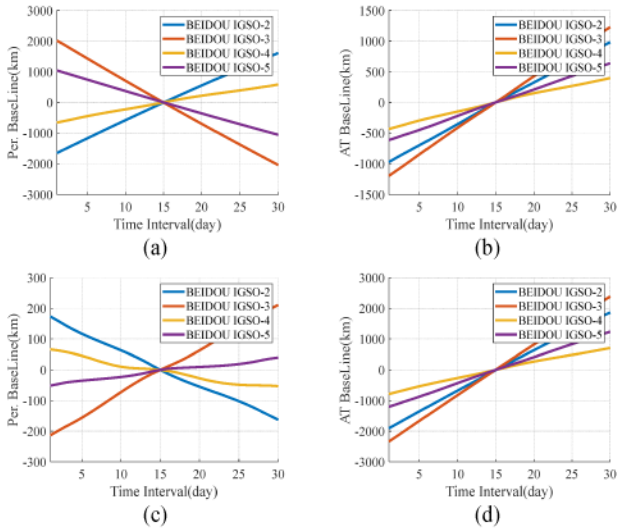

Fig. 4. Spatial baseline distribution of Beidou IGSO satellites. (a) Perpendicular baseline span near Equator. (b) Along-track baseline span near the equator. (c) Perpendicular baseline span near the pole. (d) Along-track baseline span near the pole.

III. SPATIAL SPECTRUM SYNTHESIS ALGORITHM FOR GEO SAR

Due to squint mode and 2-D baselines, the shape and shift of the spectrum of GEO SAR are different from that of LEO SAR, whose models will be derived in detail in this section. Furthermore, a modified spatial spectrum synthesis algorithm will be proposed for GEO SAR.

A. Spatial Spectrum Shape of GEO SAR

Due to the coarse resolution of GEO SAR, we use the point spread function (PSF) scattering model for radar targets. In contrast with LEO SAR, squint mode is very common in GEO SAR, so the 2-D sidelobes of PSF on the ground plane are significantly nonorthogonal. In this case, we need to use an expression of PSF under arbitrary geometry. The geometric diagram of GEO SAR is shown in Fig. 5. The reference framework takes the center of Earth O as the origin. The satellite at the aperture center moment (ACM) is located on the y-axis, and the velocity of the satellite is in the yOz plane. The vector $\vec{s}$ refers to the position of the satellite at the ACM, which points from the center of the Earth O to the position of the satellite, and the vector $\vec{u}$ is the unit vector which points from satellites to targets on the ground. For

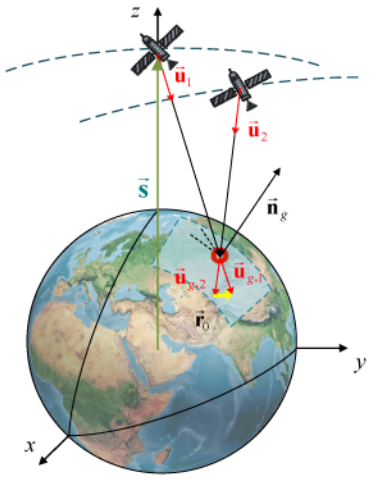

Fig. 5. GEO SAR imaging geometry.

a point target located at $\vec{\mathrm{r}}_0$ on the ground, its PSF after SAR imaging is [33]

$$h\left(\vec{\mathrm{r}};\vec{\mathrm{r}}_0\right)=\underbrace{\sigma\left(\vec{\mathrm{r}}_0\right)\exp\left(-j\frac{4\pi\left\|\vec{\mathrm{r}}_0-\vec{\mathrm{s}}\right\|}{\lambda}\right)}_{g(\vec{\mathrm{r}}_0)}\underbrace{\operatorname{sinc}\left(\frac{2B\vec{\mathrm{u}}^{\mathrm{T}}\left(\vec{\mathrm{r}}-\vec{\mathrm{r}}_0\right)}{c}\right)\operatorname{sinc}\left(\frac{2T\vec{\mathrm{v}}^{\mathrm{T}}\mathbf{P}\left(\vec{\mathrm{r}}-\vec{\mathrm{r}}_0\right)}{\lambda R}\right)}_{A(\vec{\mathrm{r}}-\mathbf{r}_0)} \tag{1}$$

where $A(\cdot)$ is the envelope of PSF and $g(\vec{\mathrm{r}}_0)$ is the scattering coefficient and phase of the target. $\sigma(\vec{\mathrm{r}}_0)$ is the complex scattering coefficient of the target. $\vec{\mathrm{r}}$ is the position of any point on the ground, $\vec{\mathrm{s}}$ and $\vec{\mathrm{v}}$ are the position and velocity of the satellite at the ACM. $\vec{\mathrm{u}}=(\vec{\mathrm{r}}_0-\vec{\mathrm{s}})/\|\vec{\mathrm{r}}_0-\vec{\mathrm{s}}\|$ is the line-of-sight (LOS) direction at the ACM. B is the radar signal bandwidth; T is the synthetic aperture time; R is the slant range; $\lambda$is the wavelength. $\mathbf{P}=\mathbf{I}-\vec{\mathrm{u}}\vec{\mathrm{u}}^{\mathrm{T}}$ is the projection matrix with $\vec{\mathrm{u}}$ as normal vector. Assuming that there are multiple scattering points on the ground, the imaging result at $\vec{\mathrm{r}}$ can be expressed as

$$Q\left(\vec{\mathrm{r}}\right)=\int h\left(\vec{\mathrm{r}};\vec{\mathrm{r}}_0\right)d\vec{\mathrm{r}}_0=A\left(\vec{\mathrm{r}}\right)\otimes g\left(\vec{\mathrm{r}}\right) \tag{2}$$

where $\otimes$ denotes convolution operation.

The 2-D spatial spectrum of the image is the result of the 2-D Fourier transform of $Q(\vec{\mathrm{r}})$ on the plane where $\vec{\mathrm{r}}$ is located. According to the properties of the Fourier transform, the spatial spectrum of the image can be expressed as

$$Q\left(\vec{\mathrm{k}}\right)=A\left(\vec{\mathrm{k}}\right)\cdot g\left(\vec{\mathrm{k}}\right) \tag{3}$$

where $\vec{\mathrm{k}}$ represents the 2-D spatial frequency (wavenumber) domain, and $A(\vec{\mathrm{k}})$ is the spatial spectrum of the envelope of PSF, which can be written as

$$A\left(\vec{\mathrm{k}}\right)=C\frac{c}{2B\vec{\mathrm{u}}^{\mathrm{T}}\cdot\vec{\mathbf{e}}_1}\frac{\lambda R}{2T\vec{\mathrm{v}}^{\mathrm{T}}\mathbf{P}\cdot\vec{\mathbf{e}}_2}$$

TABLE II
PARAMETERS OF SIMULATION OF 2-D SPATIAL SPECTRUM

Parameter	LEO SAR	GEO SAR
Semimajor Axis (km)	7153	42 164
Inclination (°)	98	53
Azimuth angle (°)	90	70
Synthetic aperture time (s)	1	506
Bandwidth (MHz)	30	30

$$\operatorname{rect}\left(\frac{c\vec{\mathbf{k}}\vec{\mathbf{e}}_1}{|2B\vec{\mathbf{u}}^{\mathrm{T}}\vec{\mathbf{e}}_1|}\right)\operatorname{rect}\left(\frac{\lambda R\vec{\mathbf{k}}\vec{\mathbf{e}}_2}{|2T\vec{\mathbf{v}}^{\mathrm{T}}\mathbf{P}\vec{\mathbf{e}}_2|}\right) \tag{4}$$

where C is a constant independent of the shape of the spectrum. $\vec{\mathbf{e}}_1$ and $\vec{\mathbf{e}}_2$ are the ground iso-Doppler and iso-range directions, respectively, which can be written as

$$\vec{\mathbf{e}}_1=\frac{\vec{\mathbf{v}}_{\mathrm{eff}}\times\vec{\mathbf{n}}_g}{\|\vec{\mathbf{v}}_{\mathrm{eff}}\times\vec{\mathbf{n}}_g\|},\qquad\vec{\mathbf{e}}_2=\frac{\vec{\mathbf{u}}_g\times\vec{\mathbf{n}}_g}{\|\vec{\mathbf{u}}_g\times\vec{\mathbf{n}}_g\|} \tag{5}$$

where $\vec{\mathbf{v}}_{\mathrm{eff}}=\vec{\mathbf{v}}^{\mathrm{T}}\mathbf{P}$ is the effective velocity of GEO SAR; $\vec{\mathbf{n}}_g$ is the normal vector of ground; $\vec{\mathbf{u}}_g=\mathbf{P}_g\vec{\mathbf{u}}$ denotes the projection of sight direction $\vec{\mathbf{u}}$ on the ground, and $\mathbf{P}_g$ denotes the projection matrix to the plane where target is located. Considering that the "stop-and-go" assumption is no longer effective in GEO SAR, we analyzed the error introduced by the approximation using the accurate positions of the radar at the transmitting and receiving moment. The relative error of the "stop-and-go" assumption is about the magnitude of 10^{-10}, which is neglectable.

According to (4), the shape of the spatial spectrum is a parallelogram formed by two rectangular window functions. The length of the two sides of the parallelogram can be expressed as

$$\vec{\mathrm{l}}_1=\frac{|2T\vec{\mathbf{v}}_{\mathrm{eff}}\vec{\mathbf{e}}_2|}{\lambda R}\cdot|\cos\langle\vec{\mathbf{e}}_1,\vec{\mathbf{e}}_2\rangle|\cdot\frac{\vec{\mathbf{v}}_g}{|\vec{\mathbf{v}}_g|}$$

$$\vec{\mathrm{l}}_2=\frac{\left|2B\vec{\mathbf{u}}^{\mathrm{T}}\vec{\mathbf{e}}_1\right|}{c}\cdot1/\sin\langle\vec{\mathbf{e}}_1,\vec{\mathbf{e}}_2\rangle\cdot\frac{\vec{\mathbf{u}}_g}{|\vec{\mathbf{u}}_g|} \tag{6}$$

where $\langle\vec{\mathbf{e}}_1,\vec{\mathbf{e}}_2\rangle$ denotes the angle between $\vec{\mathbf{e}}_1$ and $\vec{\mathbf{e}}_2$, and $\vec{\mathbf{v}}_g=\mathbf{P}_g\vec{\mathbf{v}}$ denotes the projection of effective velocity $\vec{\mathbf{v}}_{\mathrm{eff}}$ on the ground.

For traditional broadside looking SAR, it satisfies $\vec{\mathbf{v}}_{\mathrm{eff}}\perp\vec{\mathbf{u}}_g$. Thus, the two rectangular window functions of $A(\vec{\mathrm{k}})$ are orthogonal to each other, and the corresponding spatial spectrum is rectangular. However, for squint mode GEO SAR, the sidelobes are usually not orthogonal, as shown in Fig. 6. The parameters used in this simulation of the 2-D spatial spectrum are given in Table II.

B. Spatial-Spectral Shift of GEO SAR

Considering the different positions of master and slave orbits, the overlap ratio of the two spectrum envelopes is above 97%. Since the influence of the difference of LOS directions on the spectrum envelope is neglectable, we use a unified spectrum envelope $A(\vec{\mathrm{k}})$ to simplify the spectrum synthesis processing. Since the spectrum envelopes $A(\vec{\mathrm{k}})$ of the two images are the

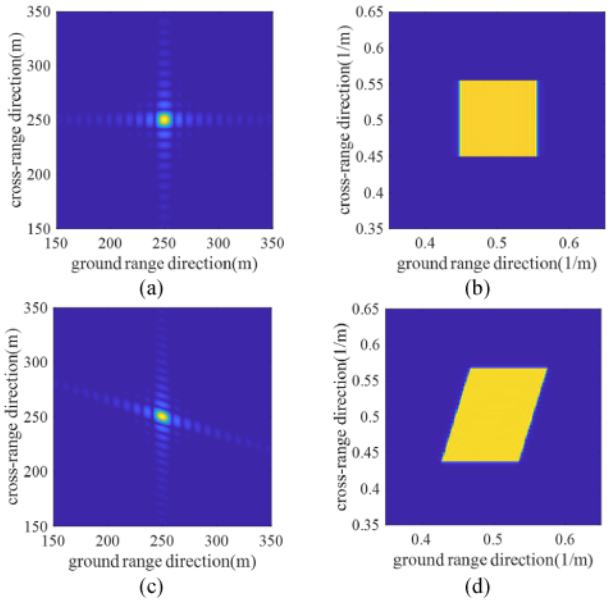

Fig. 6. 2-D spatial spectrum of LEO SAR and GEO SAR. (a) PSF of LEO SAR image. (b) 2-D spatial spectrum of LEO SAR. (c) PSF of GEO SAR image. (d) 2-D spatial spectrum of GEO SAR.

same, the spectral shift is mainly determined by the term $g(\vec{\mathrm{k}})$. In this section, we will derive the expression of $g(\vec{\mathrm{k}})$; furthermore, we will obtain the model of spectral shift.

Assuming the center of the scene is $\vec{\mathrm{r}}_0'$, we can linearly expand the slant range at the center, that is

$$\begin{aligned}\|\vec{\mathrm{r}}_0-\vec{\mathrm{s}}\| &= \|(\vec{\mathrm{r}}_0'-\vec{\mathrm{s}})+(\vec{\mathrm{r}}_0-\vec{\mathrm{r}}_0')\| \\ &\approx \|\vec{\mathrm{r}}_0'-\vec{\mathrm{s}}\|+(\vec{\mathrm{r}}_0'-\vec{\mathrm{s}})^{\mathrm{T}}(\vec{\mathrm{r}}_0-\vec{\mathrm{r}}_0')\Big/\|\vec{\mathrm{r}}_0'-\vec{\mathrm{s}}\| \\ &\approx \|\vec{\mathrm{r}}_0'-\vec{\mathrm{s}}\|+\vec{\mathrm{u}}^{\mathrm{T}}\Delta\vec{\mathrm{r}} \\ &= \|\vec{\mathrm{r}}_0'-\vec{\mathrm{s}}\|+\vec{\mathrm{u}}_g^{\mathrm{T}}\Delta\vec{\mathrm{r}} \end{aligned} \tag{7}$$

where $\Delta\vec{\mathrm{r}}=\vec{\mathrm{r}}_0-\vec{\mathrm{r}}_0'$ is the range between the target and the center of the scene.

Combining (7) and (1), we can obtain

$$\begin{aligned} g(\Delta\vec{\mathrm{r}}) &= \sigma(\vec{\mathrm{r}}_0'+\Delta\vec{\mathrm{r}})\exp\left(-j\frac{4\pi\|\vec{\mathrm{r}}_0'-\vec{\mathrm{s}}\|}{\lambda}\right) \\ &\quad \exp\left(-j2\pi\cdot\frac{2\vec{\mathrm{u}}_g^{\mathrm{T}}\Delta\vec{\mathrm{r}}}{\lambda}\right). \end{aligned} \tag{8}$$

According to the properties of the Fourier transform, g in the wavenumber domain can be expressed as

$$g\left(\vec{\mathrm{k}}\right)=\sigma\left(\vec{\mathrm{k}}-2\vec{\mathrm{u}}_g/\lambda\right)\exp\left(-j4\pi/\lambda\cdot\|\vec{\mathrm{r}}_0'-\vec{\mathrm{s}}\|\right). \tag{9}$$

Taking the spatial spectrum of scattering coefficient σ as a reference, it can be considered that the spatial spectrum of the image has a spectral shift of $\delta\vec{\mathrm{k}}=2\vec{\mathrm{u}}_g/\lambda$. Assuming that the projections of LOS of two images on the ground are $\vec{\mathrm{u}}_{g,1}$ and $\vec{\mathrm{u}}_{g,2}$, the spectrum shift between the two images is

$$\Delta\vec{\mathrm{k}}=2\left(\vec{\mathrm{u}}_{g,1}-\vec{\mathrm{u}}_{g,2}\right)/\lambda. \tag{10}$$

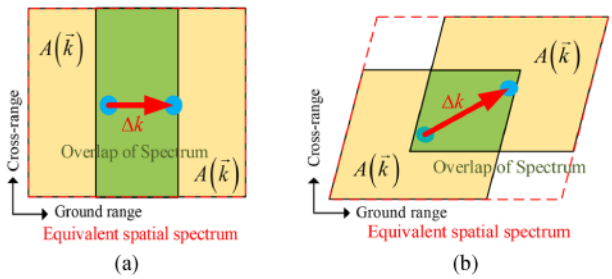

Fig. 7. Diagram of the shift of the spatial spectrum of (a) LEO SAR and (b) GEO SAR.

The geometric diagram of the spectral shift of GEO SAR is shown in Fig. 5, and the spectral shift between the images obtained by the two satellites is along the yellow arrow.

Since LEO SAR usually works in broadside looking mode, while GEO SAR usually works in squint mode, their shifts of spatial spectrum are different, as shown in Fig. 7(a) and (b). The green rectangle denotes the overlap of two spectrums and the red dotted box denotes the equivalent spatial spectrum after synthesizing.

Different from LEO SAR, due to the squint mode of GEO SAR, the spatial spectrum has two special properties.

1) The spatial spectrum of each image is a parallelogram.
2) The direction of spatial-spectral shift may be independent of the direction of parallelogram side length, since the LOS direction of GEO SAR at different data acquisition times is different, which results in the 2-D spatial-spectral shift.

C. Spatial Spectrum Synthesis Algorithm

In traditional LEO SAR, the shape and shift direction of the spectrum are relatively simple, and the spectral shift can be directly calculated. Thus, the spectrums can be shifted along the range direction and synthesized. The 2-D window function is the same as the shape of the spectrum. However, due to the two challenges mentioned above, the implementation of spectrum shift and the construction of the window function of GEO SAR are different from LEO SAR. This section completes the following two works for these two problems.

1) We use the deramping operation instead of the spectrum shifting process.
2) We construct a new window function suitable for spectrum synthesis in GEO SAR.

The algorithm flow proposed in this article is shown in Fig. 8.

1) Interpolation: This step is necessary because the original sampling interval and resolution of the image are usually similar, which is not enough for the synthesized image.

2) Deramping: Classical methods in the current literature shift the spectrums in the spatial spectrum domain directly. Because the spectral shift is generally not exactly an integer pixel, interpolation should be carried out before shifting. In this section, we propose to use deramping in the image domain to achieve spectrum shifting. The relevant principles are derived as follows.

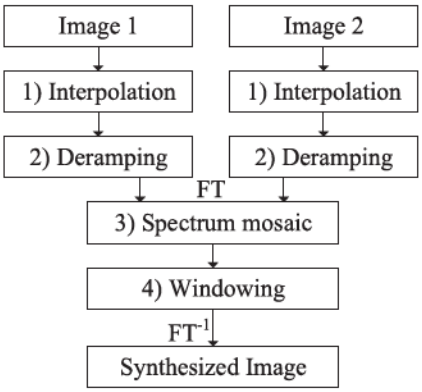

Fig. 8. Algorithm flowchart of spatial spectrum synthesis for GEO SAR.

Supposing there is only one point in the scene, the imaging results cover a small area including the main lobe and multiple sidelobes. Assuming the center of the main lobe is located at $\vec{\mathrm{x}}_0'$, the whole imaging area can be expressed as $\vec{\mathrm{x}}_0 = \vec{\mathrm{x}}_0' + \Delta\vec{\mathrm{x}}$. The size of $\Delta\vec{\mathrm{x}}$ is usually several sidelobes. The phase of the point after imaging is

$$\phi\left(\Delta\vec{\mathrm{x}}\right) = -\frac{4\pi\left\|\vec{\mathrm{x}}_0 - \vec{\mathrm{s}}\right\|}{\lambda} + \phi_0 \tag{11}$$

where ϕ_0 is the scattering phase of the target, and $\vec{\mathrm{s}}$ is the position of the satellite at ACM.

Deramping is to remove the phase corresponding to the slant range from the SAR image. Note that the slant range used for deramping at each pixel is determined by the location of itself. Similar to (7), the phase of the pixel after deramping is

$$\phi_{\text{deramp}}\left(\Delta\vec{\mathrm{x}}\right) = \phi\left(\Delta\vec{\mathrm{x}}\right) - \frac{4\pi\left\|\vec{\mathrm{x}}_0 - \vec{\mathrm{s}}\right\|}{\lambda} = -\frac{4\pi\vec{\mathrm{u}}_g^T\Delta\vec{\mathrm{x}}}{\lambda} + \phi_0. \tag{12}$$

Comparing (11) and (12), for the point target, the phase of the image is space-invariant before deramping. But after deramping, the phase of the image is linearly changed along the ground range direction. According to the properties of the Fourier transform, when the PSF of the point target is transformed into the 2-D frequency domain, a shift along the ground range direction will be generated.

According to (8) and (12), the residual phase after deramping processing is equivalent to the phase corresponding to the spatial-spectral shifts, thus we use the deramping operation instead of the spectrum shifting process.

3) Spectrum Mosaicing: Since there are spectral shifts and spectrum overlaps between SAR images, we can obtain the synthesized image with a wider bandwidth and higher resolution. The position and the overlap region of the spectrums can be predicted by the shape and shift of spectrums.

The concept of filtering is to combine two spatial spectra and balance them in the overlap region. First, the boundaries of the overlap region should be derived accurately. Considering that the spectrum overlap is a parallelogram, the mosaic window function should be a 2-D window function gradually varying along the diagonal, as shown in Fig. 9. The center of the overlap region is $2\vec{\mathrm{u}}_g/\lambda + \Delta\vec{\mathrm{k}}/2$, and the four vertices of the

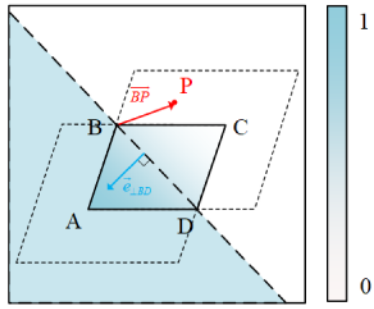

Fig. 9. Diagram of the mosaic window function.

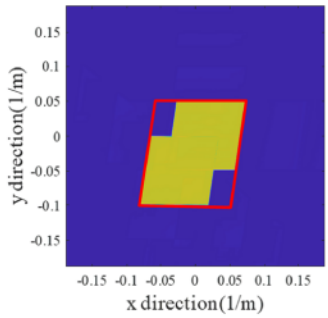

Fig. 10. SAR window function of the spatial spectrum.

parallelogram, which are *A*, *B*, *C*, *D*, can be expressed as

$$\mathrm{Vert}_{A/B/C/D} = \left(\pm\vec{\mathrm{x}}_1 \pm \vec{\mathrm{x}}_2\right) + 2\vec{\mathrm{u}}_g/\lambda + \Delta\vec{\mathrm{k}}\Big/2 \tag{13}$$

where $\vec{\mathrm{x}}_1, \vec{\mathrm{x}}_2$ are the two sides of the parallelogram, namely

$$\begin{aligned}\vec{\mathrm{x}}_1 &= \vec{\mathrm{l}}_1 - \left(\left|\Delta\vec{\mathrm{k}} - \Delta\vec{\mathrm{k}}\cdot\vec{\mathrm{v}}_g\right|\Big/\sin\left(\vec{\mathrm{e}}_1,\vec{\mathrm{e}}_2\right)\cdot\vec{\mathrm{u}}_g/|\vec{\mathrm{u}}_g| - \Delta\vec{\mathrm{k}}\right)\\ \vec{\mathrm{x}}_2 &= \vec{\mathrm{l}}_2 - \left|\Delta\vec{\mathrm{k}} - \Delta\vec{\mathrm{k}}\cdot\vec{\mathrm{v}}_g\right|\Big/\sin\left(\vec{\mathrm{e}}_1,\vec{\mathrm{e}}_2\right)\cdot\vec{\mathrm{u}}_g/|\vec{\mathrm{u}}_g|.\end{aligned} \tag{14}$$

The overlap region of spectral is synthesized by linear superposing, and the rest of the spectrum is completed by the nonoverlapping spectra. Assume that any point in the spectrum is at *P*, and $\vec{e}_{\perp BD}$ indicates a unit vector that is perpendicular to line *BD* and points to *A*. Then the mosaic window function can be expressed as

$$\text{win1} = \begin{cases} 1 - \dfrac{\overrightarrow{PA}\cdot\vec{e}_{\perp BD}}{\left|\overrightarrow{AC}\cdot\vec{e}_{\perp BD}\right|}, & \in ABCD \\ 0, & \notin ABCD \text{ and } \overrightarrow{BP}\cdot\vec{e}_{\perp BD} < 0 \\ 1, & \notin ABCD \text{ and } \overrightarrow{BP}\cdot\vec{e}_{\perp BD} > 0 \end{cases}$$

$$\text{win2} = 1 - \text{win1}. \tag{15}$$

4) Windowing: In real SAR image processing, we usually use the method of windowing in the frequency domain to suppress the sidelobes. Therefore, we windowed the equivalent spatial spectrum after synthesis. The vertices of the synthesized spatial spectrum can be predicted to construct the minimum parallelogram that can cover the synthesized spectrum, as shown in Fig. 10. After obtaining the boundary, we construct the hamming window function and operate on the synthesized spectrum.

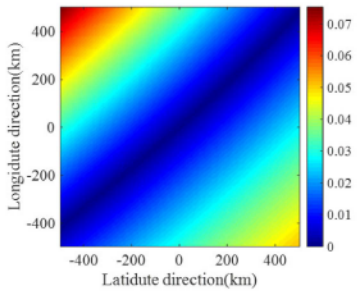

Fig. 11. Relative error introduced by the Earth's curvature.

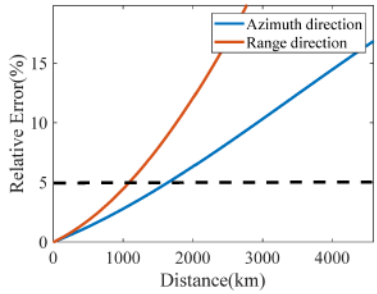

Fig. 12. Relationship between the relative error of the spectral shift amplitude and the distance of the scene.

D. Large Imaging Scene of GEO SAR

Due to the large imaging swath of GEO SAR, the imaging swath can reach 1000 km or even higher in the scanSAR mode, thus the spectral shift of different targets within the image scene may be different. There are two main reasons for the variation of the spectrum shift:

First, affected by the curvature of the Earth, the ground planes of the targets at different positions in the scene are different, which lead to the different projection of the LOS direction on the ground planes, and then results in the variation of the spectral shift. This error is introduced by (7) and reflected in the difference in projection of the LOS direction. We simulated the error of the spectral shift from the Earth's curvature, as shown in Fig. 11. The relative error introduced by the Earth's curvature is less than 7.5% over an imaging swath of 1000 km. Since the real position of the target is used in the deramping processing to substitute the spectrum shifting, it does not affect the result of the spectrum synthesis algorithm.

Second, due to the large imaging swath of GEO SAR, the range and the LOS direction of the targets at different positions in the scene are different, which leads to a nonnegligible difference in the magnitude of spectral shift. To solve this problem, we consider to divide the whole imaging scene into several subscenes. We consider the targets in any subscene to be located at the same plane and the magnitude of the spectral shift can be regarded as the same.

We study the spatial varying characteristics of the spectral shift in GEO SAR and quantitively analyze the critical value of the imaging swath to make sure that the error between the spectral shifts of the center and the boundary of the scene is within an ideal threshold. Here, we consider that an error of less than 5% can be ignored. The relationship between the relative error of the amplitude of spectral shift and the distance between the boundary and center of the scene in 2-D is shown in Fig. 12. It can be seen that the maximum scene satisfied the error threshold of 5% is no more than 1050 km in range direction and 1680 km in azimuth direction.

IV. Performance Analysis of Spatial Spectrum Synthesis in GEO SAR

In this section, we consider three main indicators including the resolution improvement factor, the amplitude fluctuation, and the critical baseline of the proposed resolution improvement algorithm for squint mode GEO SAR.

A. Resolution Improvement Factor

The resolution improvement factor is the master evaluation index of the improvement of resolution. In addition to the traditional evaluation method of the -3 dB width of the main lobe of the 2-D profiles, we also adopt the area of the resolution cell as a main indicator. According to the properties of the Fourier transform, generally, the -3 dB width in the time domain is inversely proportional to the -3 dB width in the frequency domain. Thus, the resolution improvement factor is positively related to the improvement factor of the spatial-spectral area.

For a uniform and flat area target, the geometric correlation coefficient of SAR image pairs is equal to the proportion of the overlapping area of the spatial spectrums [24]. The geometric decorrelation in squint mode can be expressed as [5]

$$\gamma_G = \underbrace{\left[1 - \frac{\left|c \cdot \Delta\vec{\mathrm{u}}^{\mathrm{T}}\vec{\mathrm{e}}_1\right|}{\left|\lambda B \cdot \vec{\mathrm{u}}_g^{\mathrm{T}}{}_g \cdot \vec{\mathrm{e}}_1\right|}\right]}_{\gamma_B} \cdot \underbrace{\left[1 - \frac{\left|R\Delta\vec{\mathrm{u}}^{\mathrm{T}}\vec{\mathrm{e}}_2\right|}{\left|T_s \cdot \vec{\mathrm{v}}_g^{\mathrm{T}}{}_g \cdot \vec{\mathrm{e}}_2\right|}\right]}_{\gamma_D} \tag{16}$$

where γ_B and γ_D, respectively, indicate the decorrelation caused by the spectrum shift in range and azimuth direction.

Thus, the improvement factor of the area of the resolution cell can be written as

$$\eta \propto \frac{2}{1+\gamma_G} \tag{17}$$

where $\propto$ indicates the positive correlation. The improvement factor of the spatial-spectral area is within 1–2, while the improvement factor of the the resolution cell area will be larger due to the irregularity of the synthesized spectrum.

In addition, improvement multiple of resolution and geometric decorrelation are contradictory. Although a larger spatial baseline can achieve better resolution improvement, it also means that the phase noise of the synthesized image is worse, which will harm the subsequent processing such as interferometry. It is worth noting that geometric decorrelation is related to the local terrain of the target, so there may be significant differences in resolution improvement factors in different regions of the scene.

TABLE III
PARAMETERS OF THE GEO SAR IMAGING SYSTEM

Parameter	Value	Parameter	Value
Bandwidth (MHz)	30	Incidence angle (°)	30
Wavelength (m)	0.24	Satellite velocity (m/s)	800
Synthetic aperture time (s)	506	Azimuth angle (°)	80
Perpendicular baseline (km)	150	Along-track baseline (km)	250

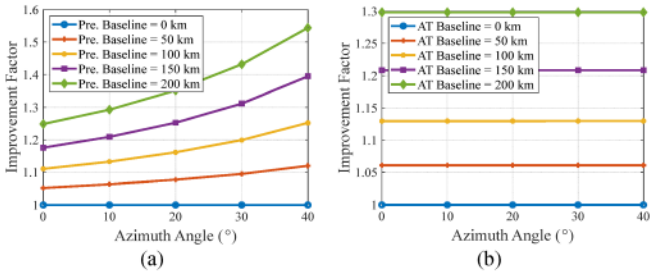

Fig. 13. Resolution improvement factor under different spatial baselines. (a) Different perpendicular baseline (along-track baseline = 0). (b) Different along-track baseline (perpendicular baseline = 0).

Here, we investigated the improvement factor of the resolution cell area under different perpendicular baselines, along-track baselines, and azimuth angles. Other parameters used in this section are given in Table III.

It can be seen from Fig. 13 that the resolution improvement factor increases with the 2-D spatial baselines, and the azimuth angle only influences the component related to the perpendicular baseline.

B. Amplitude Fluctuation

1) Isolated Point Target: Suppose there is only one isolated point target in the scene, whose elevation is $\vec{\mathrm{d}}$. Assuming that two images are obtained, the phase of the target in the master image is the scattering phase of the target after deramping, that is $\phi_1 = \phi_0$. According to the relationship between the interferometric phase and perpendicular baseline, the phase of the slave image is

$$\phi_2 = \phi_0 - \frac{4\pi \cdot \vec{\mathrm{b}}_{\perp}^{\mathrm{T}} \cdot \vec{\mathrm{d}}}{\lambda R_0} \tag{18}$$

where R_0 is the slant range between the target and master radar at the ACM.

Therefore, the phase of the synthesized image is

$$\phi_{\mathrm{syn}} = \exp(j\phi_0) + \exp\left(j\left(\phi_0 - \frac{4\pi \cdot \vec{\mathrm{b}}_{\perp}^{\mathrm{T}} \cdot \vec{\mathrm{d}}}{\lambda R_0}\right)\right)$$

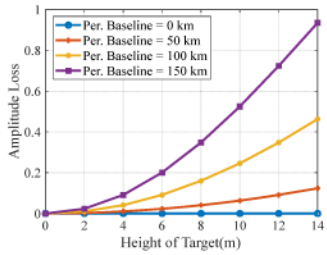

Fig. 14. Amplitude fluctuation of isolated point target under different baselines.

$$= \exp(j\phi_0) \exp\left(-j\frac{2\pi \cdot \vec{\mathrm{b}}_{\perp}^{\mathrm{T}} \cdot \vec{\mathrm{d}}}{\lambda R_0}\right) \cdot 2\cos\left(\frac{2\pi \cdot \vec{\mathrm{b}}_{\perp}^{\mathrm{T}} \cdot \vec{\mathrm{d}}}{\lambda R_0}\right). \tag{20}$$

That is to say, after image synthesis, a fluctuation will be introduced to the image amplitude, which can be expressed as

$$\eta = 1 - \cos\left(2\pi \cdot \vec{\mathrm{b}}_{\perp}^{\mathrm{T}} \cdot \vec{\mathrm{d}} \Big/ (\lambda R_0)\right). \tag{21}$$

The amplitude fluctuation of isolated point target under different baselines is shown in Fig. 14. The amplitude fluctuation is related to both error of the target elevation and perpendicular baseline. Considering that the precision of current global DEM accuracy reaches 5 m (i.e., TerraSAR DEM product), the tolerable perpendicular baseline is relatively large. The amplitude loss is within 20% in the case of a perpendicular baseline of 150 km.

2) Uniform Area Target: The influence of terrain fluctuation on spectrum synthesis in a broadside looking mode was analyzed by Prati and Rocca [22]. The terrain fluctuation within several meters in a resolution cell will cause amplitude loss of the synthesized image.

Assuming that k is the number of SAR images and there is terrain fluctuation $\delta(\vec{\mathrm{r}}_0)$ at the position $\vec{\mathrm{r}}_0$ along the range direction, substitute $\|\vec{\mathrm{r}}_0 + \delta(\vec{\mathrm{r}}_0) - \vec{\mathrm{s}}_k\|$ for $\|\vec{\mathrm{r}}_0 - \vec{\mathrm{s}}\|$ in (2), and we can obtain the kth SAR image as

$$Q_k(\vec{\mathrm{r}}) = \int A(\vec{\mathrm{r}} - \vec{\mathrm{r}}_0)\sigma(\vec{\mathrm{r}}_0) \exp\left(-j\frac{4\pi}{\lambda}\left(\vec{\mathrm{u}}_k^{\mathrm{T}}(\vec{\mathrm{r}}_0 - \vec{\mathrm{r}} + \delta(\vec{\mathrm{r}}_0))\right)\right) d\vec{\mathrm{r}}_0. \tag{22}$$

The synthesized image can be expressed as (19) shown at the bottom of this page. It can be seen that the synthesis results of the two images are obtained by a weighted average of each pixel in the resolution cell.

Generally, a resolution cell of a uniform area target contains several scattering points with the same amplitude and independent identically distributed phase. Therefore, we can express the

$$I = Q_1(\vec{\mathrm{r}}) + Q_2(\vec{\mathrm{r}}) = \int A(\vec{\mathrm{r}} - \vec{\mathrm{r}}_0)\,\sigma(\vec{\mathrm{r}}_0)\underbrace{2\cos\left(\frac{2\pi}{\lambda R_0}\vec{\mathrm{b}}_{\perp}^{\mathrm{T}}(\vec{\mathrm{r}}_0 - \vec{\mathrm{r}} + \delta(\vec{\mathrm{r}}_0))\right)\exp\left(-j\frac{4\pi}{\lambda}\left(\frac{\vec{\mathrm{u}}_1^{\mathrm{T}} + \vec{\mathrm{u}}_2^{\mathrm{T}}}{2}(\vec{\mathrm{r}}_0 - \vec{\mathrm{r}} + \delta(\vec{\mathrm{r}}_0))\right)\right)}_{F(\delta(\vec{\mathrm{r}}_0))} d\vec{\mathrm{r}}_0. \tag{19}$$

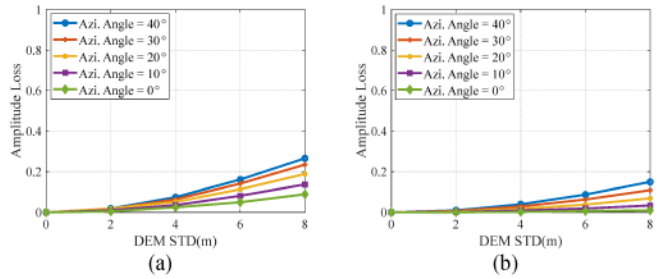

Fig. 15. Influence of terrain fluctuation on amplitude loss under different azimuth angles. (Along-track baseline = 0 km). (a) Perpendicular baseline is 150 km. (b) Perpendicular baseline is 50 km.

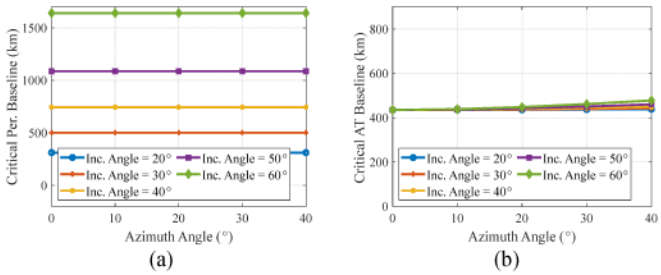

Fig. 16. Critical spatial baseline of GEO SAR. (a) Perpendicular baseline. (b) Along-track baseline.

amplitude fluctuation of the area target statistically as

$$\eta = 1 - \frac{E\left[\int \sigma\left(\vec{\mathbf{r}}_0\right) F\left(\delta\left(\vec{\mathbf{r}}_0\right)\right) d\vec{\mathbf{r}}_0\right]}{E\left[\int \sigma\left(\vec{\mathbf{r}}_0\right) d\vec{\mathbf{r}}_0\right]}. \tag{23}$$

We simulate the amplitude loss of synthesized images at different resolutions with different perpendicular baselines and azimuth angles, as shown in Fig. 15. The amplitude loss gets worse with the increasing azimuth angle, which indicates the terrain fluctuation should be taken into account in high squint mode.

C. Critical Baseline

According to (16), similar to LEO SAR, the geometric decorrelation of GEO SAR images in squint mode is also composed of baseline decorrelation and Doppler decorrelation. The critical baseline is determined by $\gamma_B \geq 0$ and $\gamma_D \geq 0$, which yields

$$\begin{aligned} \left|\Delta\vec{\mathbf{u}}^{\mathrm{T}}\vec{\mathbf{e}}_1\right| &\leq \frac{\lambda B \cdot \left|\vec{\mathbf{u}}_g^{\mathrm{T}}{}_g \cdot \vec{\mathbf{e}}_1\right|}{c} \\ \left|\Delta\vec{\mathbf{u}}^{\mathrm{T}}\vec{\mathbf{e}}_2\right| &\leq \frac{T_s \left|\vec{\mathbf{v}}_g^{\mathrm{T}}{}_g \cdot \vec{\mathbf{e}}_2\right|}{R}. \end{aligned} \tag{24}$$

We simulated critical perpendicular and along-track baselines according to (24), as shown in Fig. 16. The results show that for GEO SAR, for a specific synthetic aperture length, the critical perpendicular baseline depends on the incidence angle but hardly varies with the azimuth angle. The critical value of the along-track baseline hardly varies with the incidence angle and azimuth angle.

TABLE IV
PROPERTY OF RESOLUTION IMPROVEMENT IN POINT TARGET SIMULATION EXPERIMENT

	-3 dB width of master image/m	-3 dB width of synthesized image/m	Resolution improvement factor	Theoretical value
***x*-axis**	9.07	7.20	1.26	1.30
***y*-axis**	9.07	6.13	1.48	1.57

TABLE V
PROPERTY OF RESOLUTION IMPROVEMENT IN POINT TARGET SIMULATION EXPERIMENT WITH NONIDEAL FACTORS

	-3 dB width of master image/m	-3 dB width of synthesized image/m	Resolution improvement factor	Theoretical value
***x*-axis**	8.93	7.18	1.24	1.30
***y*-axis**	9.07	6.14	1.48	1.57

V. SIMULATION AND EXPERIMENT

To verify the validity of the theory above, we conducted a computer simulation of the point target and area target and carried out an equivalent experiment based on the measured data of Beidou IGSO navigation satellites.

A. Point Target Simulation

The parameters used in the point target simulation are given in Table III. The backprojection (BP) imaging algorithm is adopted in this simulation. The azimuth and ground range resolution of the original image are both 8.86 m. According to the analysis in Section IV, the critical perpendicular and along-track baselines in this case are 501.7 km and 435.9 km, respectively. Following the process described in Section III, the synthesized imaging results of the point target without considering nonideal factors are shown in Fig. 17.

Fig. 18(a) and (b) presents the windowed master image and the synthesized image. It is obvious that compared with the master image, the point target after spectrum synthesizing has a narrower main lobe. Since the hamming window will influence the energy distribution of the main and sidelobes, the resolution improvement factor should be evaluated without windowing. The area of resolution cell is improved from 55.11 to 31.14 m^2. The simulated resolution improvement factor is 1.77, which is larger than the theoretical value 1.50 obtained by (16). This is because there are gaps in the synthesized spectrum. Thus, it is more appropriate to measure the theoretical resolution improvement factor with the area improvement of the minimum convex hull of the synthesized spectrum, which is 1.81 in this case. The results show that the spatial spectrum synthesis algorithm has the ability of super resolution, and the price is enhancing sidelobes and even producing grating lobes.

Fig. 18(a) and (b) presents the 2-D profiles of the windowed images. We evaluated the -3 dB width of the main lobe of the 2-D profiles of two images and compared them with the theoretical values obtained from the critical spatial baseline. It can be seen from Table IV that the error between the experimental value and

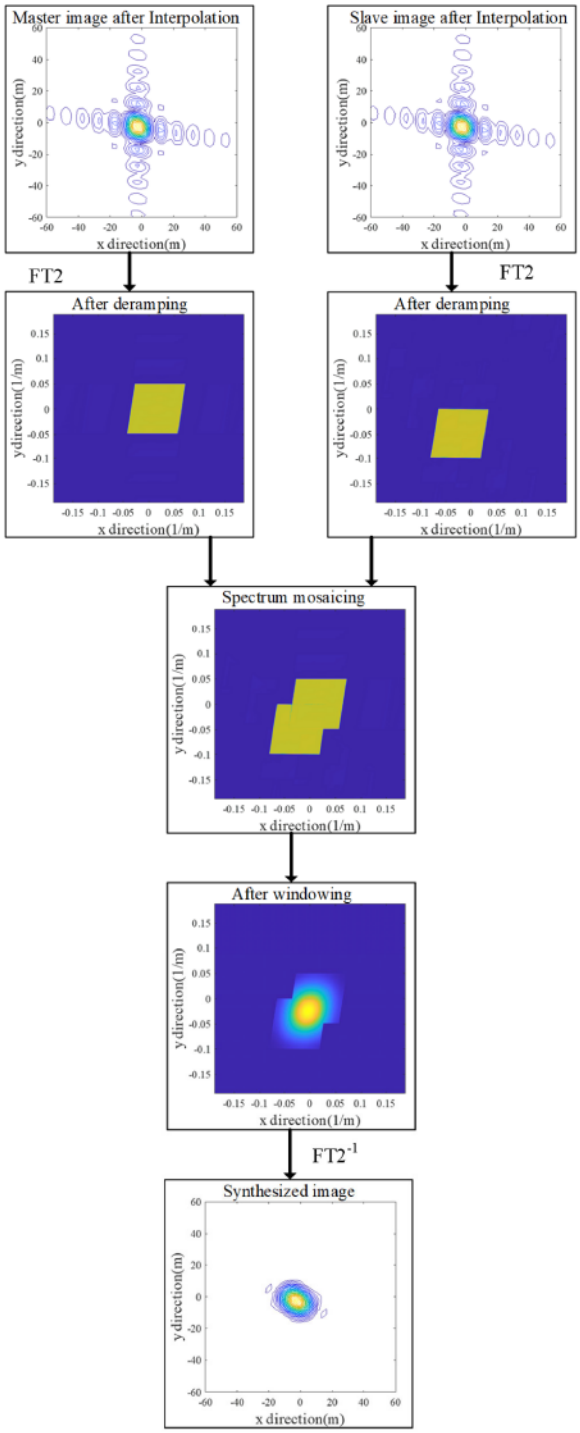

Fig. 17. Simulation results of spectrum synthesized imaging of point target.

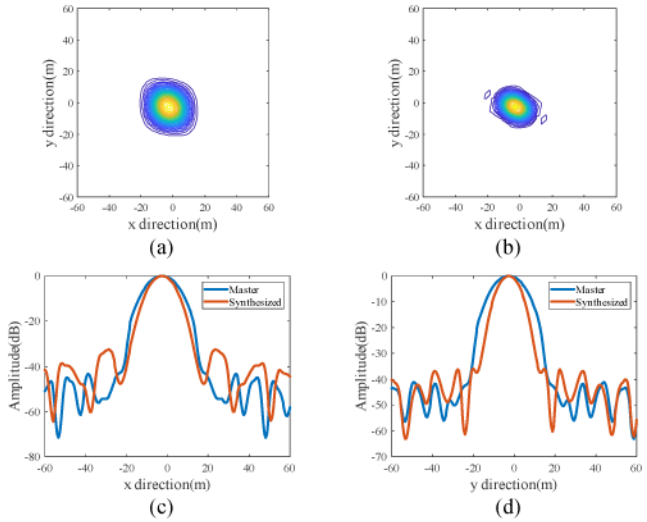

Fig. 18. Comparison between (a) windowed master image and (b) synthesized image. (c) Profiles along the x-axis. (d) Profiles along the y-axis.

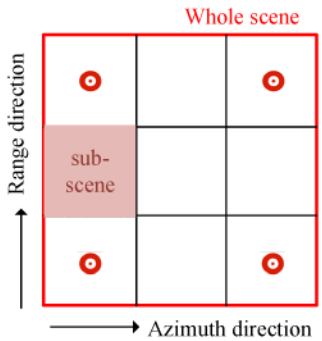

Fig. 19. Partition of the whole scene and subscenes.

the theoretical value is within 6%, which verifies the proposed algorithm.

We expand the scene to an imaging swath over 3000 km. The size of the subscenes is set to 1000 km × 1000 km to make sure the difference of the spectral shift is neglectable. The spectrum synthesis of SAR images is completed by block processing based on the analysis above. The whole scene and subscenes are shown in Fig. 19. We divide the scene into nine parts and operate the spectrum synthesizing on point targets located in boundary parts. Detailed results of this simulation are shown in Appendix.

B. Impact of Nonideal Factors

Nonideal factors such as temporal decorrelation and atmospheric turbulence could inject strong noise and give to the image a smoothing effect even if many point targets could gain resolution.

1) Temporal Decorrelation: Temporal decorrelation is determined by the temporal baselines and the standard deviation of the target random walk in the scene, according to the model of temporal decorrelation [34]

$$\hat{\gamma}(t) = (\gamma_0 - \gamma_\infty) e^{-\frac{t}{\tau}} + \gamma_\infty$$
$$\tau = \frac{2}{\sigma_r^2}\left(\frac{\lambda}{4\pi}\right)^2 \tag{25}$$

where γ_0 is the initial coherence, γ_∞ is the long-term coherence, τ is the rate of the temporal decorrelation, and σ_r is the standard deviation of the target random walk.

As for the urban area, we obtained by analyzing and fitting the SAR images of TerraSAR-X in urban Beijing, according to

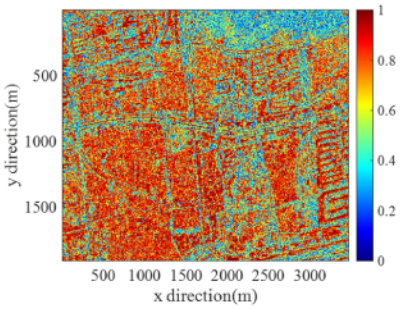

Fig. 20. InSAR coherence of TerraSAR-X data in urban Beijing area.

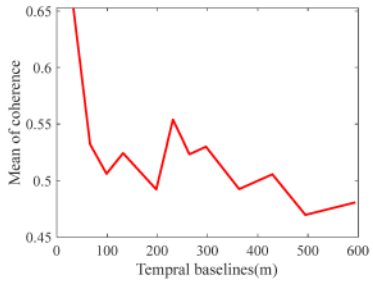

Fig. 21. Changing of mean coherence of the images.

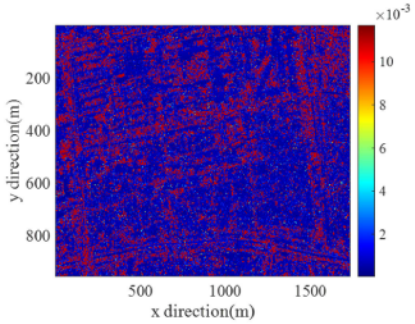

Fig. 22. Fitting results of random walk standard deviation σ_r in urban Beijing area.

the model of temporal decorrelation. We used ten SAR images of TerraSAR-X, and one of the coherences of InSAR pairs is shown in Fig. 20.

Then we calculated the sequence of mean coherence of the images, as shown in Fig. 21.

Finally, fitting the parameter σ_r according to the model of temporal decorrelation from the variation of image coherence. We obtained the deviation of the target random walk in the urban scene, as shown in Fig. 22. The mean random walk standard deviation σ_r of urban area target is about 0.057.

Based on the analysis above, we add temporal decorrelation with standard deviation σ_r and 1-day temporal baselines to the image in the processing of imaging to simulate the impact of temporal decorrelation.

As for atmospheric turbulence, we used the spectrum model of Kolmogorov to simulate the impact of turbulence, which is

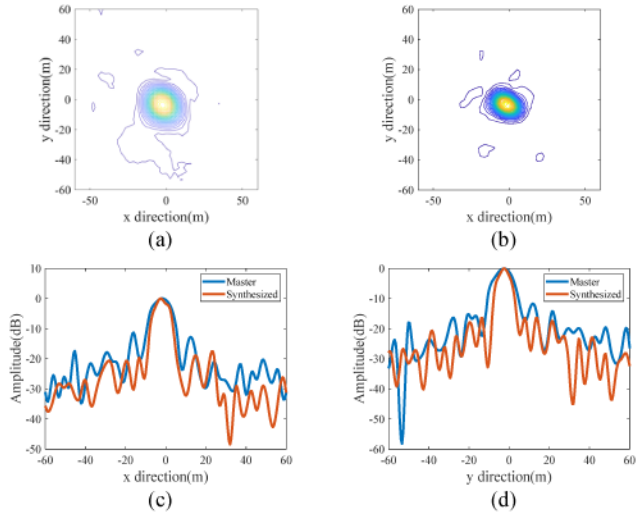

Fig. 23. *L*-band GEO SAR images with nonideal factors: comparison between (a) windowed master image and (b) synthesized image. (c) Profiles along the *x*-axis. (d) Profiles along the *y*-axis.

suitable for small-scale turbulence. The Kolmogorov model can be expressed as [35]

$$\Phi(\kappa) = \frac{\Gamma(a+1)}{4\pi} \sin[(a-1)\pi/2] C_n^2 \kappa^{-a-2} = 0.033 C_n^2 \kappa^{-11/3} \tag{26}$$

where Φ is the power spectral density of the turbulence; $\Gamma(\cdot)$ is the Gamma function; a is the parameter of different turbulent power spectrum models; C_n^2 is the atmospheric structure constant of refractive index; κ is the spatial beam.

Compared with the *X*- and *C*-band, the effect of atmospheric turbulence on the *L*-band is much slighter. The effect of atmospheric turbulence on *L*-band SAR is negligible in practice. We used the standard deviation refractive index of 0.3, which indicates the square root of the power of turbulence, to simulate the impact of atmospheric turbulence.

Considering the impact of nonideal factors, the results of the simulation are shown in Fig. 23. It can be seen that temporal decorrelation and atmospheric turbulence have little effect on the *L*-band GEO SAR system with a repeated time of one day. The deviation of improvement of the –3 dB width of the main lobe and the area of resolution between the simulation and theoretical value is still less than 6%, as shown in Table V. It verifies the effectiveness of the spectrum synthesis algorithm for GEO SAR under the case of existing nonideal factors, such as temporal decorrelation and atmospheric turbulence.

However, for SAR operating in low orbit, the repeated time is generally 20 days or even more, and the impact of temporal decorrelation on the SAR images and the processing of synthesizing cannot be ignored. It can be found that after adding the influence of nonideal factors on SAR images of *L*- and *X*-band LEO SAR, the defocused target appeared in the synthesized image, as shown in Appendix B. Based on the simulation and analysis above, the effectiveness and advantages of spectrum synthesis algorithm used in *L*-band GEO SAR are verified.

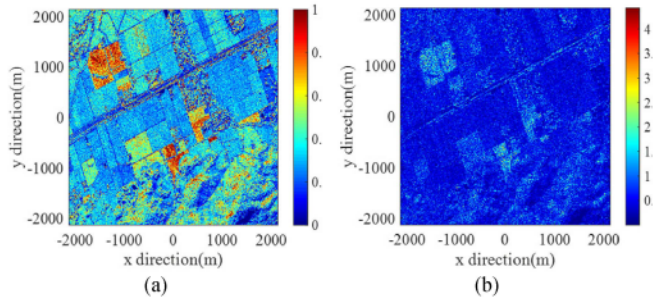

Fig. 24. Input and simulated image. (a) Input intensity map. (b) Simulated image.

TABLE VI
SPATIAL BASELINES OF THREE CASES IN AREA TARGET SIMULATION EXPERIMENT

Cases	Number of images	Baselines (Perpendicular/Alongtrack)/km
a	3	0/0, -350/-350, 350/350
b	3	0/0, -350/250, 350/-250
c	5	0/0, -350/-350, 350/350, -350/250, 350/-250

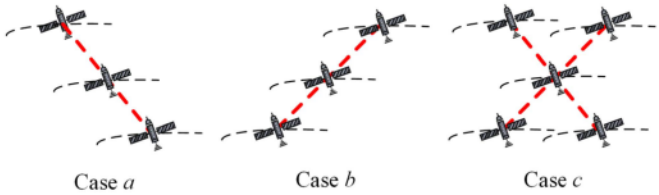

Fig. 25. Schematic diagram of the distribution of baselines in area target simulation experiment.

C. Area Target Simulation

In this section, for area target simulation, we selected an intensity map of a measured SAR image of a relatively flat area, which is shown in Fig. 24(a). The image has a size of 1600 × 1600, with a pixel interval of 2.67 m. The intensity map was used as a backscattering coefficient to generate SAR echo data.

Then, we used the imaging method in the previous section and the simulated image with the original resolution is shown in Fig. 24(b).

To verify the proposed algorithm, we set up three cases with different baselines and different numbers of images. The details of the baseline distributions are given in Table VI, and the schematic diagram is shown in Fig. 25.

In order to intuitively observe the resolution improvement performance of the image, we selected two typical scenes in the whole image (as shown in Fig. 26) for comparison. It can be clearly seen that, compared with the original master image, the boundary lines in the scene after synthesizing are much clearer and the image resolution is significantly improved. The different distribution of baselines could result in different directions of the resolution improvement. To be specific, for cases *a* and *b*, the resolution of images is mainly improved along left-down to right-up and left-up to right-down direction, respectively. For case *c*, the resolutions are improved in two dimensions.

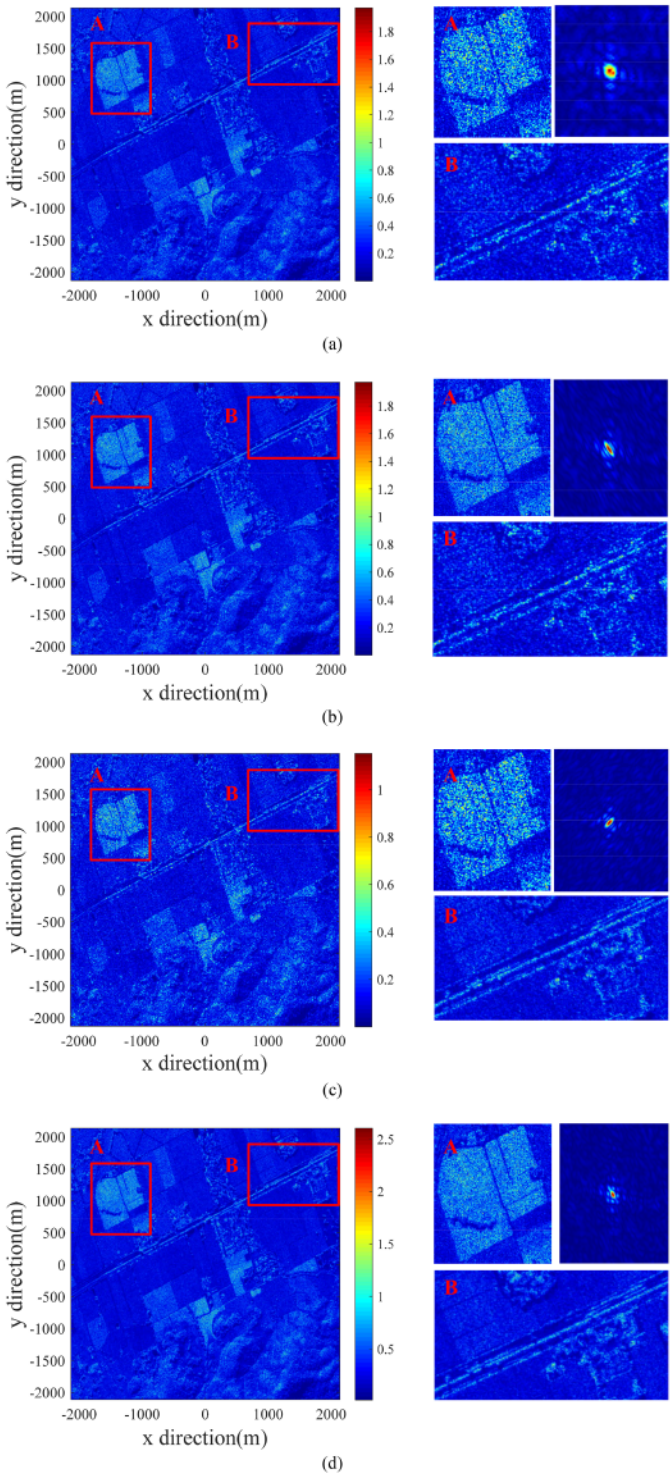

Fig. 26. Simulation result of synthesized imaging algorithm of area target. (a) Master image. Synthesized image of (b) case *a*, (c) case *b*, and (d) case *c*.

To qualitatively analyze the resolution improvement performance of the algorithm, we also added an isolated strong point target in the target scene. We evaluated the improvement of the -3 dB width of the main lobe in two dimensions and the

TABLE VII
PERFORMANCE OF RESOLUTION IMPROVEMENT IN AREA TARGET SIMULATION EXPERIMENT

	-3dB width of *x*-axis/m	Simulated/ Theoretical improvement factor	-3dB width of *y*-axis/m	Simulated/ Theoretical improvement factor	Area of resolution cell/m^2	Simulated/ Theoretical improvement factor	Image entropy
Master image	8.87	-	9.00	-	62.36	-	6.36
3 images (case *a*)	4.20	2.11/2.40	3.47	2.59/2.60	17.09	3.65/3.67	7.08
3 images (case *b*)	3.93	2.26/2.40	4.40	2.05/2.00	17.68	3.53/3.67	7.08
5 images (case *c*)	3.80	2.33/2.40	3.60	2.50/2.60	12.45	5.43/5.57	7.39

TABLE VIII
PROPERTY OF RESOLUTION IMPROVEMENT IN BEIDOU EQUIVALENT EXPERIMENT

	-3 dB width of master image/m	-3 dB width of synthesized image/m	Resolution improvement factor	Theoretical value
***x*-axis**	27.23	20.40	1.33	1.26
***y*-axis**	5.32	5.02	1.06	1.08

resolution cell area, as given in Table VII . In all three cases, the simulated improvement factors of -3 dB width of the main lobe are consistent with their theoretical value. The improvement of the area of the resolution cell is consistent with the amplification of the convex hull area of the spatial spectrum with a relative error of less than 4%. In addition, the image entropy improves with the area of the synthesized spectrum, which indicates the increase of the information in the image, according to Shannon information theory [36]. The results verify the algorithm and evaluation model.

D. Equivalent Experiment Based on Beidou IGSO Satellites

Since the GEO SAR satellite is still in the stage of demonstration and development, there is no GEO SAR satellite in orbit at present. In addition to the similarity in the operation orbit, GEO SAR and Beidou IGSO navigation satellites are also similar in the aspect of transmitting frequency (both are *L*-band), signal bandwidth (GEO SAR: 30 MHz; Beidou IGSO satellite: 20.46 MHz), and revisit period ($<$ 1 day). Thus, we could use Beidou IGSO navigation satellite data for equivalent experimental verification.

The equivalent experiment was carried out in March 2016 in Beijing, China. The geometry of the experiment is bistatic, that is, the ground-based antenna receives the echo of the scene from navigation satellite signals. The imaging processing mainly includes synchronizing and BP imaging [21]. The resolution of the Beidou SAR image is 3.5 m $\times$ 15 m (azimuth direction $\times$ ground range direction).

We selected the measured data of the IGSO4 satellite, and the optical image and SAR image of the observed area are shown in Fig. 27 .

First, we analyzed the distribution of the spatial baseline of the Beidou IGSO4 satellite in 29 days. The 15th day's track was selected as a reference track and the spatial baseline in elevation and along-track direction of the remaining repeated tracks was calculated relative to the reference track, as shown in Fig. 28. The

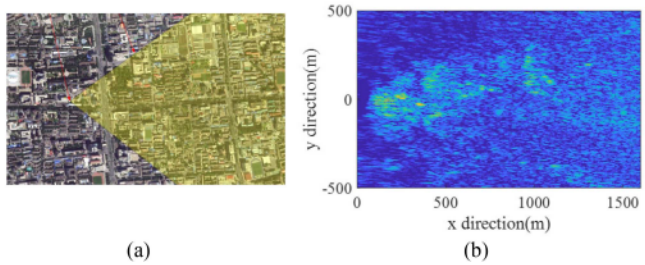

Fig. 27. (a) Optical image and (b) SAR image of Beidou equivalent experiment.

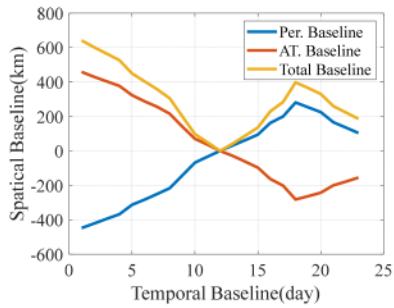

Fig. 28. Spatial baseline distribution of Beidou IGSO4 satellites.

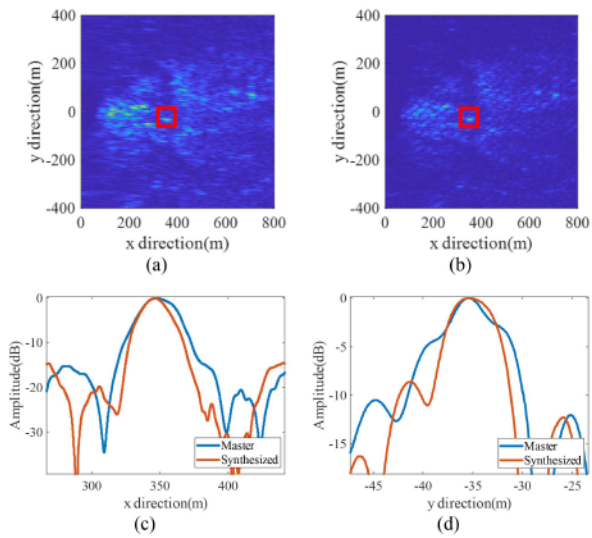

Fig. 29. Experimental result of synthesized imaging algorithm of Beidou IGSO satellite. (a) Original master image. (b) Synthesized image. Profiles of strong scattering point along (c) *x*-axis and (d) *y*-axis.

TABLE IX
PERFORMANCE OF RESOLUTION IMPROVEMENT IN LARGE SCENE SIMULATION EXPERIMENT

	-3 dB width of master image/m	-3 dB width of synthesized image/m	Simulated/ Theoretical improvement factor	Area of primary resolution cell/m^2	Area of synthesized resolution cell/m^2	Simulated/ Theoretical improvement factor
A	12.27 14.94	7.73 12.80	1.59/1.78 1.16/1.24	115.56	58.67	1.97/2.17
B	16.53 13.34	13.87 8.26	1.19/1.11 1.61/1.66	90.67	51.56	1.76/1.84
C	10.13 13.06	8.80 8.27	1.15/1.15 1.58/1.60	48.00	26.67	1.80/1.81
D	10.40 14.14	8.00 10.13	1.30/1.27 1.40/1.34	48.00	33.78	1.42/1.63

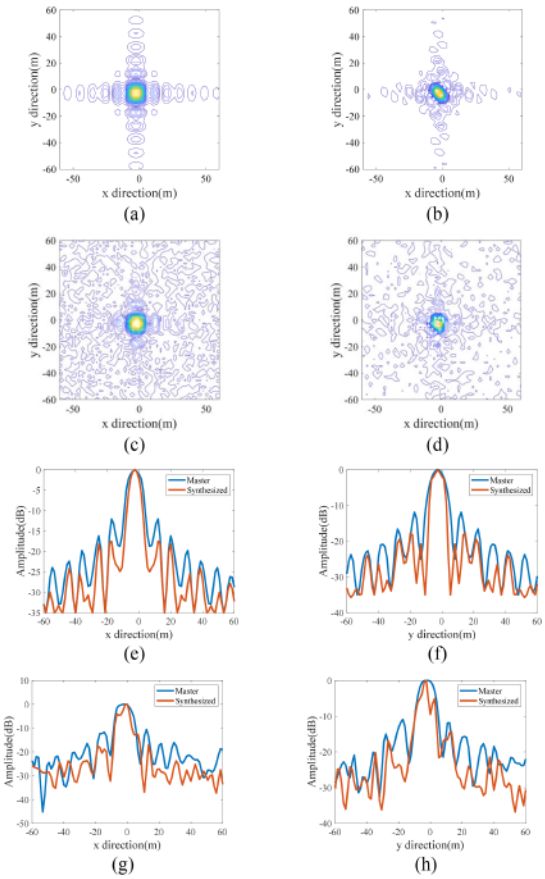

Fig. 30. *L*-band LEO SAR images: comparison between master images and synthesized images: (a), (b) without nonideal factors and (c), (d) with nonideal factors. Profiles along the *x*- and *y*-axis of SAR images: (e), (f) without nonideal factors and (g), (h) with nonideal factors.

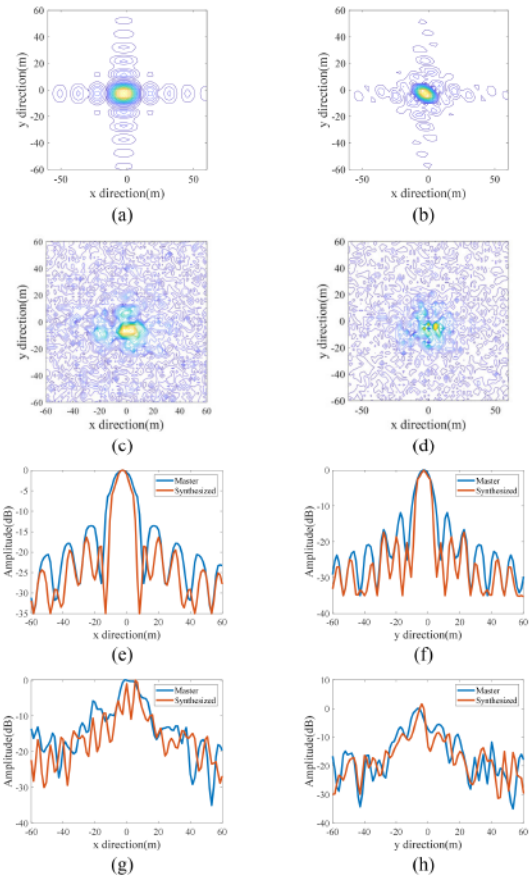

Fig. 31. *X*-band LEO SAR images: comparison between master images and synthesized images: (a), (b) without nonideal factors and (c), (d) with nonideal factors. Profiles along the *x*- and *y*-axis of SAR images: (e), (f) without nonideal factors and (g), (h) with nonideal factors.

perpendicular and along-track baseline span of Beidou IGSO4 satellite can reach more than 400 km, and it has the potential to achieve 2-D resolution improvement of images based on spatial spectrum synthesis.

We selected two images with a time interval of two days for spatial spectrum synthesis, and the perpendicular and along-track baselines are 67.88 km and 70.32 km, respectively. The critical perpendicular and along-track baselines in this case are 256.89 km and 893.59 km, respectively. The data processing in Section III is adopted in this section. The synthesized image and the original master image of a part of the scene are shown in Fig. 29(a) and (b). It can be seen that the resolution of the SAR image improves evidently. In order to quantitatively evaluate the resolution improvement factor, we selected a strong scattering point target shown in the red box of the image to analyze its 2-D sidelobes, as shown in Fig. 29(c) and (d).

It can be seen from Table VIII that the error between the experimental value and the theoretical value is within 5%. The area of resolution cell is improved from 115.88 to 89.44 m^2. The simulated resolution improvement factor is 1.30, which is consistent with the theoretical value 1.25. The results verify the improvement of the 2-D resolution of SAR images and the validity of the algorithm and theoretical analysis in this article.

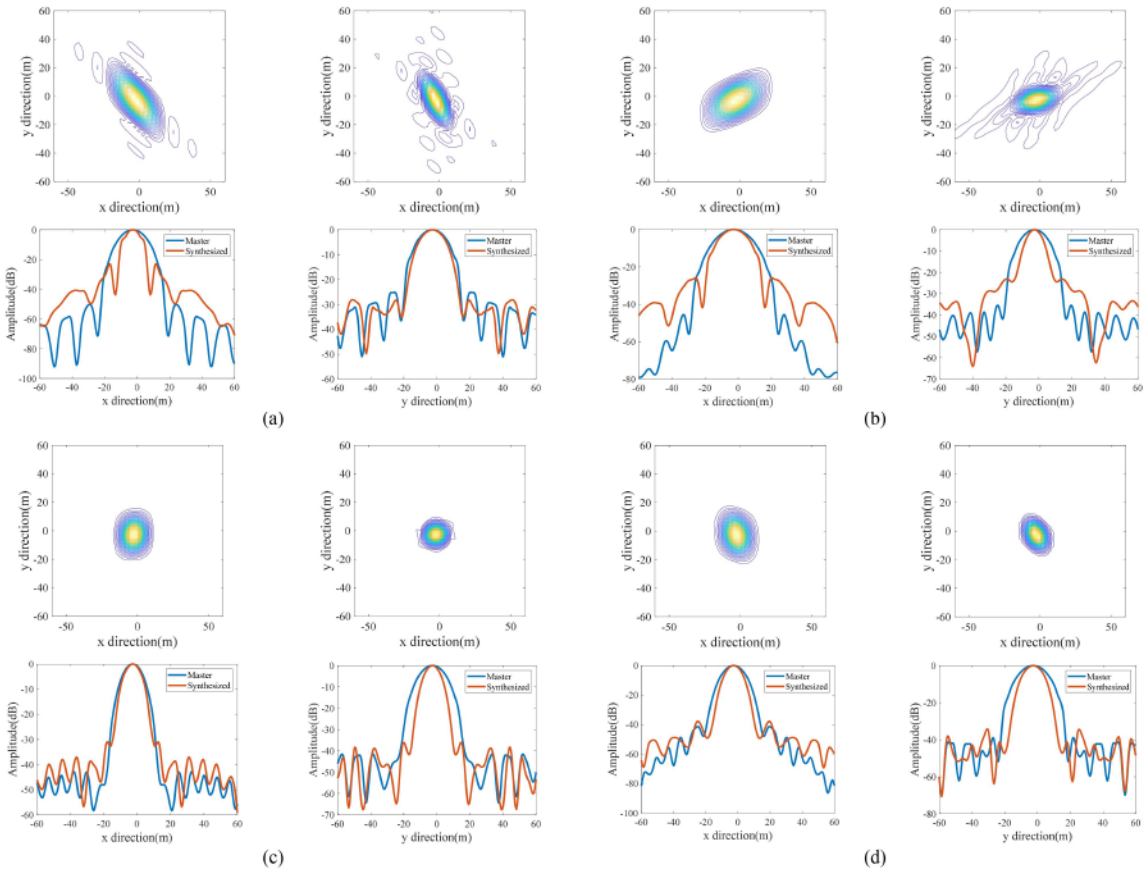

Fig. 32. Comparison between windowed master image and synthesized image, and profiles along the x- and y-axis at four positions in a large scene. (a) Point A. (b) Point B. (c) Point C. (d) Point D.

VI. Conclusion

Aiming at the problems of squint mode and 2-D spatial baselines for GEO SAR, this article studies spatial spectrum synthesis algorithms to improve 2-D resolution. The vector model of the shape and shift of the GEO SAR spectrum is derived. The synthesis algorithm flow is improved by the deramping operation. The evaluation models including the resolution improvement factor, the amplitude fluctuation, and the critical baseline are constructed. The effectiveness of the proposed algorithm is verified by simulation experiments of point target and area target and equivalent experiments based on the measured data of Beidou IGSO navigation satellites. The results of the simulation and experiment show that the proposed algorithm is suitable for the GEO SAR platform in the presence of squint, and the impact of nonideal factors on the synthesis algorithm of L-band GEO SAR is negligible. Different resolution improvement factors can be achieved through spatial baseline settings based on the performance analysis presented in this article.

Spatial spectrum synthesis algorithms are highly dependent on the topography of the scene; therefore, further research on spatial spectrum synthesis under different terrain will be carried out in the future. In addition, for the irregular synthesized spectrum, the method of suppressing the sidelobes will be studied.

Appendix

A. Simulation of Nonideal Factors for LEO SAR

For L-band SAR operating in low orbit, the repeated time is generally 20 days or even more, and the impact of temporal decorrelation on the SAR images and the processing of synthesizing cannot be ignored. It can be found that after adding the influence of nonideal factors on SAR images of L-band LEO SAR, the defocused target appeared in the synthesized image, as shown in Fig. 30.

Furthermore, we simulate the application of the spectrum synthesis algorithm in X-band low-orbit SAR. Compared with the L-band, atmospheric turbulence and temporal decorrelation have greater effects on X-band SAR images. It can be found that after adding the influence of nonideal factors on SAR images of X-band LEO SAR, the worse defocused target appeared in the synthesized image, as shown in Fig. 31. Based on the simulation and analysis above, the effectiveness and advantages of spectrum synthesis algorithm used in L-band GEO SAR are verified.

B. Simulation of Big Scenes for GEO SAR

Fig. 32 presents the windowed master image and the synthesized image of the point targets, and profiles along the x- and y-axis of the targets in a large scene. We evaluate the results

using the methods mentioned in the article. The results show that the spatial spectrum synthesis algorithm can be used for large imaging scenes in GEO SAR.

We evaluated the -3 dB width of the main lobe of the 2-D profiles and the area of the resolution cell of the two images, and compared them with the theoretical values obtained from the critical spatial baseline. It can be seen from Table IX that the error between the experimental value and the theoretical value is within 10%, which verifies the proposed algorithm.

REFERENCES

[1] T. Long, C. Hu, Z. Ding, X. Dong, W. Tian, and T. Zeng, "Three dimensional deformation retrieval in GEO D-InSAR," in *Geosynchronous SAR: System and Signal Processing*. New York, NY, USA: Springer, 2018, pp. 273–290.

[2] Accessed: Feb. 17, 2024. [Online]. Available: https://spacenews.com/China-launches-first-geosynchronous-orbit-radar-satellite/

[3] K. Tomiyasu, "Synthetic aperture radar in geosynchronous orbit," in *Proc. New Mex. State Univ. Proc. Syn. Aperture Radar Technol. Conf.*, 1978, pp. 42–45.

[4] S. N. Madsen, C. Chen, and W. Edelstein, "Radar options for global earthquake monitoring," in *Proc. IEEE Int. Geosci. Remote Sens. Symp.*, Toronto, ON, Canada, 2002, vol. 3, pp. 1483–1485.

[5] Z. Chen, C. Hu, X. Dong, Y. Li, W. Tian, and S. Hobbs, "Coherence-based geosynchronous SAR tomography employing formation flying: System design and performance analysis," *IEEE Trans. Geosci. Remote Sens.*, vol. 59, no. 9, pp. 7165–7179, Sep. 2021.

[6] S. Hobbs, C. Mitchell, B. Forte, R. Holley, B. Snapir, and P. Whittaker, "System design for geosynchronous synthetic aperture radar missions," *IEEE Trans. Geosci. Remote Sens.*, vol. 52, no. 12, pp. 7750–7763, Dec. 2014.

[7] Y. Tian et al., "Theoretical analysis and verification of time variation of background ionosphere on geosynchronous SAR imaging," *IEEE Geosci. Remote Sens. Lett.*, vol. 12, no. 4, pp. 721–725, Apr. 2015.

[8] Y. Ji, Y. Zhang, Z. Dong, Q. Zhang, D. Li, and B. Yao, "Impacts of ionospheric irregularities on L-band geosynchronous synthetic aperture radar," *IEEE Trans. Geosci. Remote Sens.*, vol. 58, no. 6, pp. 3941–3954, Jun. 2020.

[9] J. R. Rodon, A. Broquetas, A. M. Guarnieri, and F. Rocca, "Geosynchronous SAR focusing with atmospheric phase screen retrieval and compensation," *IEEE Trans. Geosci. Remote Sens.*, vol. 51, no. 8, pp. 4397–4404, Aug. 2013.

[10] Z. Ding et al., "An autofocus back projection algorithm for GEO SAR based on minimum entropy," *IEEE Trans. Geosci. Remote Sens.*, vol. 60, 2022, Art. no. 5226114.

[11] Q. Chen, W. Liu, G.-C. Sun, X. Chen, L. Han, and M. Xing, "A fast cartesian back-projection algorithm based on ground surface grid for GEO SAR focusing," *IEEE Trans. Geosci. Remote Sens.*, vol. 60, 2021, Art. no. 5217114.

[12] H. An, J. Wu, K. C. Teh, Z. Sun, and J. Yang, "Geosynchronous spaceborne–Airborne bistatic SAR imaging based on fast low-rank and sparse matrices recovery," *IEEE Trans. Geosci. Remote Sens.*, vol. 60, 2021, Art. no. 5207714.

[13] P. A. Rosen et al., "Synthetic aperture radar interferometry," *Proc. IEEE*, vol. 88, no. 3, pp. 333–382, Mar. 2000.

[14] A. Reigber and A. Moreira, "First demonstration of airborne SAR tomography using multibaseline L-band data," *IEEE Trans. Geosci. Remote Sens.*, vol. 38, no. 5, pp. 2142–2152, Sep. 2000.

[15] Y. Li, C. Hu, and D. Ao, "Rapid surface large-change monitoring by repeat-pass GEO SAR multibaseline interferometry," *IEEE Geosci. Remote Sens. Lett.*, vol. 19, 2020, Art. no. 4002905.

[16] G. Krieger et al., "TanDEM-X: A satellite formation for high-resolution SAR interferometry," *IEEE Trans. Geosci. Remote Sens.*, vol. 45, no. 11, pp. 3317–3341, Nov. 2007.

[17] V. Ignatenko, P. Laurila, A. Radius, L. Lamentowski, O. Antropov, and D. Muff, "ICEYE microsatellite SAR constellation status update: Evaluation of first commercial imaging modes," in *Proc. IEEE Int. Geosci. Remote Sens. Symp.*, Waikoloa, HI, USA, 2020, pp. 3581–3584.

[18] Jet Propulsion Lab. NASA, "Global earthquake satellite system: A 20-year plan to enable earthquake prediction," California Inst. Technol., Pasadena, CA, USA, 2003.

[19] S. E. Hobbs and A. Monti-Guarnieri, "Geosynchronous continental land-atmosphere sensing system (G-Class): Persistent radar imaging for earth science," in *Proc. IEEE Int. Geosci. Remote Sens. Symp.*, Valencia, Spain, 2018, pp. 8621–8624.

[20] S. N. Madsen, W. Edelstein, L. D. Didomenico, and J. Labrecque, "A geosynchronous synthetic aperture radar; for tectonic mapping, disaster management and measurements of vegetation and soil moisture," in *Proc. IEEE Int. Geosci. Remote Sens. Symp. Scanning Present Resolving Future*, Sydney, NSW, Australia, 2001, pp. 447–449.

[21] C. Hu, B. Zhang, X. Dong, and Y. Li, "Geosynchronous SAR tomography: Theory and first experimental verification using Beidou IGSO satellite," *IEEE Trans. Geosci. Remote Sens.*, vol. 57, no. 9, pp. 6591–6607, Sep. 2019.

[22] C. Prati and F. Rocca, "Improving slant-range resolution with multiple SAR surveys," *IEEE Trans. Aerosp. Electron. Syst.*, vol. 29, no. 1, pp. 135–143, Jan. 1993.

[23] F. Gatelli, A. M. Guamieri, F. Parizzi, P. Pasquali, C. Prati, and F. Rocca, "The wavenumber shift in SAR interferometry," *IEEE Trans. Geosci. Remote Sens.*, vol. 29, no. 4, pp. 855–865, Jul. 1994.

[24] D. Massonnet, "Capabilities and limitations of the interferometric cartwheel," *IEEE Trans. Geosci. Remote Sens.*, vol. 39, no. 3, pp. 506–520, Mar. 2001.

[25] H. Xu, Y. Zhou, and C. Li, "An algorithm based on spectrum shift estimation for improving range resolution using distributed spaceborne interferometric SAR," *Acta Electronica Sinica*, vol. 31, no. 12, pp. 1790–1794, 2003.

[26] J. Zheng, H. Song, X. Shang, and Y. Wu, "An algorithm based on spectrum shift for improving range resolution using GEO Spaceborne/Airborne multistatic SAR," *J. Electron. Inf. Technol.*, vol. 32, no. 8, pp. 1863–1868, 2010.

[27] D. Pastina, F. Santi, and M. Bucciarelli, "MIMO distributed imaging of rotating targets for improved 2-D resolution," *IEEE Geosci. Remote Sens. Lett.*, vol. 12, no. 1, pp. 190–194, Jan. 2015.

[28] Y. Cheng, S. Zhang, B. Zhao, and C. Hu, "SA-based orbital design method for GEO-BiSAR resolution improvement," in *Proc. 32nd Gen. Assem. Sci. Symp. Int. Union Radio Sci.*, 2017, pp. 1–4.

[29] D. Mao et al., "Forward-looking geometric configuration optimization design for spaceborne-airborne multistatic synthetic aperture radar," *IEEE J. Sel. Topics Appl. Earth Observ. Remote Sens.*, vol. 14, pp. 8033–8047, 2021.

[30] C. Hu, X. Li, T. Long, and Y. Gao, "GEO SAR interferometry: Theory and feasibility study," in *Proc. IET Int. Radar Conf.*, Xi'an, China, 2013, pp. 1–5.

[31] Z. Ding, W. Yin, T. Zeng, and T. Long, "Radar parameter design for geosynchronous SAR in squint mode and elliptical orbit," *IEEE J. Sel. Topics Appl. Earth Observ. Remote Sens.*, vol. 9, no. 6, pp. 2720–2732, Jun. 2016.

[32] X. Dong, C. Hu, W. Tian, M. Bian, T. Zhang, and T. Long, "Experiment validation of inclined geosynchronous SAR foucusing using Beidou IGSO satellite," in *Proc. IEEE Int. Geosci. Remote Sens. Symp.*, Milan, Italy, 2015, pp. 3750–3753.

[33] C. Hu, T. Long, T. Zeng, F. Liu, and Z. Liu, "The accurate focusing and resolution analysis method in geosynchronous SAR," *IEEE Trans. Geosci. Remote Sens.*, vol. 49, no. 10, pp. 3548–3563, Oct. 2011.

[34] A. Monti-Guarnieri, M. Manzoni, D. Giudici, A. Recchia, and S. J. R. S. Tebaldini, "Vegetated target decorrelation in SAR and interferometry: Models, simulation, and performance evaluation," *Remote Sens.*, vol. 12, no. 16, 2020, Art. no. 2545.

[35] A. N. Kolmogorov, "The local structure of turbulence in incompressible viscous fluid for very large Reynolds," *Proc. Roy. Soc. London. A, Math. Phys. Sci.*, vol. 30, 1941, Art. no. 301.

[36] C. E. Shannon, "A mathematical theory of communication," *ACM SIGMOBILE Mobile Comput. Commun. Rev.*, vol. 5, no. 1, pp. 3–55, 2001.

Xinyan Chen was born in Shandong, China, in 1998. She received the B.S. degree in intelligence science and technology from the School of Information Science and Technology from Sun Yat-Sen University, Guangdong, China, in 2019. She is currently working toward the Ph.D. degree in information and communication engineering with the Department of Electronics and Information Engineering, Beijing Institute of Technology, Beijing, China.

Her research interests include synthetic aperture radar (SAR) systems and signal processing, tomography SAR interferometry techniques, and super-resolution imaging technology in GEO SAR.

Zhiyang Chen (Member, IEEE) was born in Fujian, China, in 1993. He received the B.S. degree in electronic science and technology from the Department of Electronic Engineering, Tsinghua University, Beijing, China, in 2016, and the Ph.D. degree in information and communication engineering from the School of Information and Electronics (SIE), Beijing Institute of Technology (BIT), Beijing, China, in 2021.

He is currently a Postdoctoral Researcher with SIE, BIT. His research interests include geosynchronous synthetic aperture radar satellite formation design, SAR interferometry, and SAR tomography.

Yuanhao Li (Member, IEEE) received the B.S. degree in information engineering and the Ph.D. degree in information and communication engineering from the Beijing Institute of Technology (BIT), Beijing, China, in 2012 and 2018, respectively.

From 2016 to 2017, he was a Visiting Researcher with the Dipartimento di Elettronica e Informazione, Politecnico di Milano, Italy. In 2018, he was a Research Scientist with the Radar Research Lab, BIT, Beijing. Between 2018 to 2021, he was a Postdoctoral Researcher with the Department of Geoscience and Remote Sensing, Delft University of Technology, Delft, The Netherlands. He is currently an Associate Professor with the School of Information and Electronics, BIT, Beijing. His research interests include radar system design and signal processing, InSAR/D-InSAR technique, and radar altimeter constellations.

Dr. Li was a recipient of the Chinese Institute of Electronics Youth Conference Excellent Paper Award in 2014.

Cheng Hu (Senior Member, IEEE) received the B.S. degree in electronic engineering from the National University of Defense Technology, Changsha, China, in 2003, and the Ph.D. degree in target detection and recognition from the Beijing Institute of Technology (BIT), Beijing, China, in 2009.

He was a Visiting Research Associate with the University of Birmingham, Birmingham, U.K., for 15 months from 2006 to 2007. Since 2009, he has been with the School of Information and Electronics, BIT, and was promoted to a Full Professor in 2014, a Doctoral Supervisor, and the Vice Director of the Radar Research Lab. He has authored more than 60 SCI-indexed journal articles and more than 100 conference articles. His main research interests include new concepts for synthetic aperture radar imaging and the biological detection radar systems and signal processing.

Xichao Dong (Member, IEEE) received the B.S. degree in electrical engineering and the Ph.D. degree in target detection and recognition from the Beijing Institute of Technology (BIT), Beijing, China, in 2008 and 2014, respectively.

From 2011 to 2013, he was a Research Assistant with the Centre for Terrestrial Carbon Dynamics, University of Sheffield, Sheffield, U.K. From 2014 to 2017, he was in a postdoctoral position with the School of Information and Electronics, BIT. Since 2017, he has been with the School of Information and Electronics, BIT, where he was promoted to an Associate Professor in 2021. His research interests include geosynchronous synthetic aperture radar and weather radar.

Dr. Dong was a recipient of the IEEE CIE International Radar Conference Excellent Paper Award in 2011 and the Chinese Institute of Electronics Youth Conference Poster Award in 2014.

Stephen Hobbs (Member, IEEE) received the B.S. degree in mathematics and physics from Trinity College, Cambridge University, Cambridge, U.K., in 1980, and the Ph.D. degree in ecological physics from the Cranfield Institute of Technology, Bedford, U.K., in 1986, with the focus on kite anemometry.

He leads the Space Group at Cranfield University, Cranfield, U.K. He has active research work in sensor systems for space and remote sensing applications. He has more than 30 years experience of teaching space engineering at the postgraduate level and planning and reviewing taught courses. His technical expertise includes spaceborne radar (technology and applications), space system engineering, "clean space," atmospheric science, sensor system/instrumentation development, signal processing, and mathematical modeling. He has led major research projects for a variety of funding agencies, including most recently the European Space Agency.

https://dspace.org/

Improving 2D resolution in geosynchronous SAR via spatial spectrum synthesis: method and verification

Chen, Xinyan; Chen, Zhiyang; Li, Yuanhao; Hu, Cheng; Dong, Xichao ...

2024-02-01
Institute of Electrical and Electronics Engineers (IEEE)
https://doi.org/10.1109/JSTARS.2024.3361165
Chen X, Chen Z, Li Y, et al., (2024) Improving 2D resolution in geosynchronous SAR via spatial spectrum synthesis: method and verification. IEEE Journal of Selected Topics in Applied Earth Observations and Remote Sensing, Volume 17, February 2024, pp. 5847-5863

Downloaded from a DSpace repository. https://dspace.org/